Are Volatiles from Subducted Ridges on the Pampean Flat Slab Fracking the Crust? Evidence from an Enhanced Seismicity Catalogue

A. Maharaj[1], S. Roecker[1], P. Alvarado[2], S. Trad[2], S. Beck[3], and D. Comte[4]

[1]*Department of Earth and Environmental Sciences, Rensselaer Polytechnic Institute, Troy, NY*
[2]*Universidad Nacional de San Juan, CONICET-UNSJ, Argentina*
[3]*Department of Geosciences, University of Arizona, Tucson, AZ, USA*
[4]*Departamento de Geofisica, Universidad de Chile, Santiago, Chile*

Key Points:

- Automatically generated catalogues of seismicity in the Pampean flab slab show parallel lineaments of seismicity in the Nazca plate.
- The lineaments are reflected in the bearing and spacing of seamount chains seen in Nazca plate bathymetry.
- Correlation of mantle seismicity with that in the crust suggests that subducted ridges release volatiles that induce crustal seismicity.

Abstract

Seamounts and ridges are often invoked to explain subduction-related phenomena, but the extent of their involvement remains controversial. An analysis of seismicity in the region of the Pampean flat slab through an application of an automated catalogue generation algorithm resulted in 143,716 local earthquake hypocenters, 35,924 of which are associated with at least 12 arrival time estimates, at least 3 of which are from S waves, along with a total of 12,172 focal mechanisms. Several new features related to the subduction of the Juan Fernandez Ridge were discovered, including: (1) a series of parallel lineaments of seismicity in the subducted Nazca plate separated by about 50 km and striking about 20°, and (2) a strong spatial correlation between these deeper (> 80 km depth) regions of intense seismicity and concentrations of activity in the crust almost directly above it. Focal mechanisms of the deeper events are almost exclusively normal, while those in the crust are predominantly reverse. The deeper lineaments mirror the origination and spacing of several seamount chains seen on the Nazca plate, suggesting that these patterns are caused by these same types of features at depth. This would imply that relatively minor features persist as slab anomalies long after they are subducted. The correlation of these deeper features with seismicity in the mid to lower crust suggests a genetic relation between the two. We postulate that volatiles from the subducted ridges percolate into the South American crust and induce seismicity essentially by fracking it.

Plain Language Summary

The ocean floor has many anomalous features such as seamounts and ridges that are believed to have profound consequences for subduction zones. Some of these effects can be illuminated by determining the locations and mechanisms of earthquakes associated with them. Seismic data collected near one of these features, the Juan Fernandez Ridge beneath South America, were analyzed with an automated catalogue generation routine to significantly increase the

number of well constrained earthquake locations from this area. Plots of these new locations reveal patterns in and around the subducted ridge that mirror the distribution of minor ridges on the Nazca plate, suggesting that the consumption of similar ridges is responsible for this activity. Moreover, these patterns are reflected in the patterns of earthquakes in the South American crust directly above them, also suggesting a genetic relationship. We hypothesize that volatiles such as water or carbon dioxide are being released by these subducted ridges, migrating through the South American mantle, and essentially fracking the mid to lower crust by increasing pore pressure.

1 Introduction

The subduction of bathymetric irregularities such as seamounts and ridges are generally considered to play a role in a variety of phenomena related to the subduction process such as flat slab generation (e.g., Ramos et al. 2002; Rosenbaum & Mo 2011), intraplate coupling (e.g., Scholz & Small, 1997), and tectonic erosion (e.g., Stern, 2020). However, the significance of these irregularities in these processes is unresolved. For example, while lower density bathymetric highs intuitively should contribute to flattening by adding buoyancy to the subducting slab, several studies suggest that the size of these features is insufficient to initiate slab flattening (e.g., Martinod et al., 2005; Espurt et al., 2008; Gerya et al., 2009). There are also several examples of regions where such features subduct without causing slab flattening, as well as regions where flat slabs show no correlation with known bathymetric highs (Rosenbaum & Mo, 2011; Skinner & Clayton, 2013; Manea et al., 2017).

The extent to which bathymetric highs interact with the overriding plate is similarly controversial. A subducted seamount may be decapitated shortly after subduction and accreted onto the forearc, becoming part of the accretionary prism (e.g., Yang et al. 2022), or remain intact for some distance along the plate interface, denting and uplifting the margin and preventing frontal accretion in its wake (Dominguez et al., 1998, 2000; Rosenbaum & Mo, 2011; Ruh et al., 2016). Seamounts may also enhance accretion when thick loose sediment exists in flanking flexural moats (Staudigel et al., 2010; Clarke et al., 2018). Watts et al. (2010) suggest that the timing of decapitation depends on multiple factors such as the thickness of the subduction channel relative to the height of the feature, the strength of the overriding plate relative to that of the feature, the internal structure of the feature (e.g., presence of volcanic cores) and whether the buoyancy of the feature is locally or regionally compensated. Wang & Bilek (2011) argue that, rather than full decapitation, seamounts are more likely to have small pieces break off as they are dragged against the upper plate. While the extent to which these features retain their status as coherent entities after they are subducted is unclear, Bonnet et al., (2019) infer that an exhumed seamount at the Siah Kuh massif in Southern Iran was subducted intact to 30 km depth. They also suggest that the overall paucity of exhumed seamounts could be interpreted as evidence that seamounts remain mostly intact after they are subducted.

As a seamount moves through the subduction channel, networks of thrust faults, sub-vertical strike-slip, and normal faults can form within the overriding plate, with a transition from thin- to thick-skinned deformation as basement faults are reactivated (Dominguez et al., 1998, 2000; Wang & Bilek, 2011; Rosenbaum & Mo, 2011; Marcaillou et al., 2016; Ruh et al., 2016). Subduction erosion and underplating can occur as the feature collides with the accretionary prism and drags material into the subduction channel (e.g., von Huene et al., 2004; Gravelau et al., 2012) or in the wake of the feature as sediments slide along the faulted

upper plate (e.g., Dominguez et al., 1998, 2000; Gravelau et al., 2012; Marcaillou et al., 2016). Higher rates of subduction erosion also have been linked to the subduction of bathymetric highs (e.g., Hampel et al., 2004; Navarro-Aràanguiz et al., 2022).

Seamounts are also believed to be responsible for transporting large amounts of fluid into the subduction channel (e.g., Pommier & Evans, 2017). Chesley et al. (2021) found that lithosphere with seamounts in the Hikurangi Margin, New Zealand, transported up to 4.7 times more fluid into the subduction zone than smoother oceanic lithosphere, which can subsequently be transported to the overriding plate, mantle wedge and deep mantle. This increase in fluid leads to more fluid migration at the subduction interface, increasing pore pressure and further fracturing the upper plate (e.g., Marcaillou et al., 2016). Hydrofracturing plays a role in basal erosion in conjunction with abrasion as the feature is dragged beneath the upper plate (e.g., Gravelau et al., 2012). In the long term, basal erosion may lead to thinning of the upper plate and thickening of the subduction channel in the region of the feature (e.g., Marcaillou et al., 2016) which will in turn affect the timing of decapitation of the seamount (Watts et al., 2010).

Bathymetric highs are often presumed to enhance interplate coupling with the overriding plate and thus affect seismicity by acting as either a nucleating asperity or arresting barrier to earthquake rupture and propagation. As asperities, they may locally increase stress and friction and thus increase the interplate coupling that generates large earthquakes (e.g., Watts et al., 2010; Rosenbaum & Mo, 2011; Wang & Lin, 2022). Contreras-Reyes & Carrizo (2011) suggested that the buoyancy of bathymetric highs can increase the normal stresses at the subduction interface to a minimum of 10-50 MPa, while Scholz & Small (1997) estimate that large seamounts can increase normal stress by as much as 200 MPa. Acting as barriers, bathymetric highs may increase normal stress to the point where friction and the yield shear stress is too high to allow slip and rupture (Watts et al., 2010; Contreras-Reyes & Carrizo, 2011). Other studies have suggested that seamounts tend to undergo ductile deformation and creep rather than brittle failure, so stress is not accumulated but rather released aseismically as numerous small earthquakes (e.g., Watts et al., 2010; Rosenbaum & Mo, 2011; Bonnet et al., 2019). Wang and Bilek (2011) postulate that the crosscutting fracture networks that develop as a seamount is subducted result in a heterogenous stress regime where internal fractures fail randomly and suggest this as a mechanism by which seamounts creep aseismically.

Increased fluid release by seamounts has also been proposed to reduce friction and interplate coupling, thus contributing to aseismic creep (e.g., Mochizuki et al., 2008). Alternatively, the increased pore pressure could favor rupture propagation (Contreras-Reyes & Carrizo, 2011). Wang & Lin (2022) suggest that mechanical strength can vary both in front of and behind a seamount, varying interplate coupling and seismicity locally around a seamount. Contreras-Reyes & Carrizo (2011) propose that the thickness of the subduction channel above seamounts partially controls whether seamounts act as barriers or asperities as a thicker channel could smooth the subduction interface and promote rupture propagation.

Clearly there are many more conjectures than certainties regarding the roll of seamounts in subduction. A major obstacle to clarifying these questions is the diminishing ability to resolve these smaller features with increasing depth (Wang & Bilek, 2011; Bonnet et al., 2019). One of the more robust sources of information we have about the state of the interplate contact in subduction zones comes from precisely located seismicity that can be used to infer either brittle failure or the existence of mineralogical phase transactions (such as from dehydration or decarbonation), either of which can reveal an anomalous combination of pressure, temperature, and/or lithology at depth. As part of an ongoing project to investigate the lithospheric evolution of South America in the central Andes (e.g., Roecker et al., 2021), we reanalyzed existing seismic data sets from networks located above the Pampean flat slab (Figure 1). Of significance to this study, some of these networks are positioned above a highly active region of seismicity that, given its location and bearing, is generally considered to be associated with subduction of the Juan Fernandez Ridge (JFR). Here we discuss the implications of a new and more comprehensive seismic event catalogue generated from these data sets for the subduction of the JFR and related bathymetric anomalies.

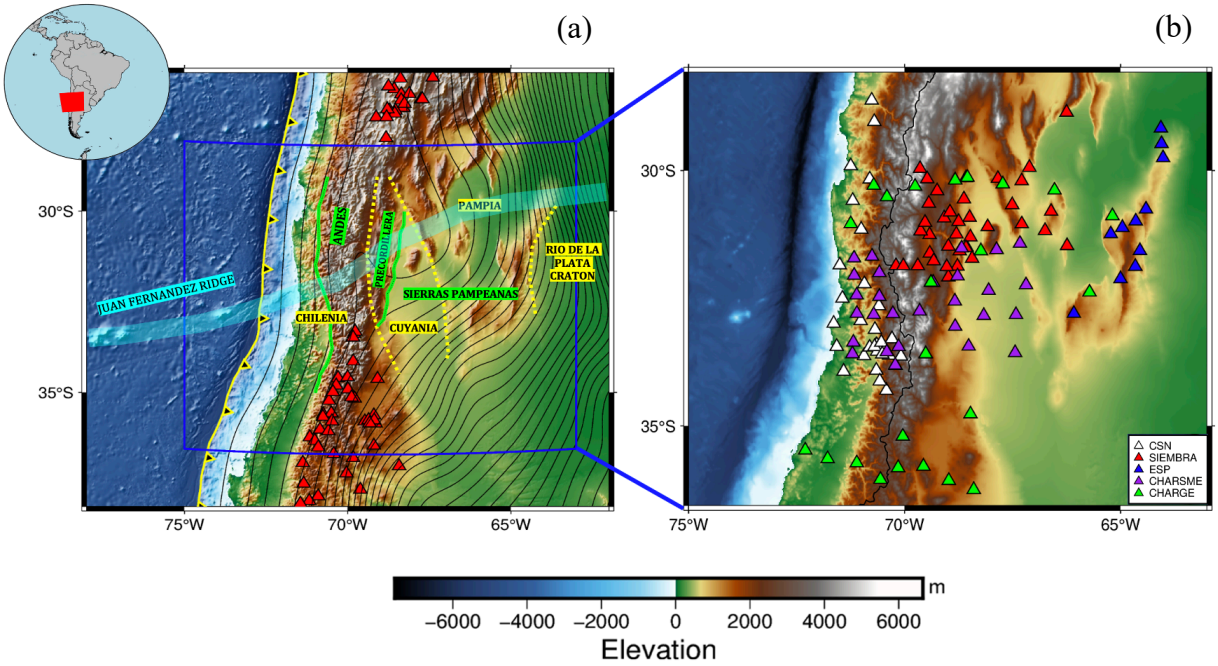

Figure 1. (a) Map showing area of study with geologic provinces (green lines) and terranes (yellow dashed lines) based on Marot et al. (2014) and Linkimer et al. (2020). Projection of the Juan Fernandez Ridge (light blue line) is based on Bello-González et al. (2018). Volcanoes (red triangles) and convergent plate boundary (yellow line with triangles) between the Nazca Plate and South American plate are from Gómez et al. (2019). Slab Contours in intervals of 20 km depth (black lines) are from Hayes (2018). Blue box locates the region shown in (b). (b) Map showing the locations of the seismic stations used in this study, color coded by their associated network. Elevation is indicated in the palette at the bottom of the figure.

2 Tectonic setting

The Pampean flat slab is located beneath the South American plate between 28°S and 33°S (Figure 1a) where the ~40 Ma Nazca plate converges with the South American plate at an oblique angle and a rate of ~7 cm/yr (e.g., DeMets et al. 2010; Manea et al., 2017). In this region, the Nazca plate subducts at a 30° angle to a depth of ~100 km, beyond which it extends more or less horizontally for ~300 km before resuming a steep descent into the mantle (e.g.,

Cahill & Isacks, 1992; Anderson et al., 2007; Hayes, 2018; Manea et al., 2017; Linkimer et al., 2020). The flattening of the slab began in the late Miocene at ~5 Ma and is associated with an eastward migration and eventual cessation of volcanic activity in the area (Kay & Mpodozis, 2002; Ramos et al., 2002). The flat slab also appears to be responsible for the eastward migration of deformation inland to the Precordillera and the Sierra Pampeanas (e.g., Jordan et al., 1983; Ramos et al. 1996; Ramos et al., 2002; Anderson et al., 2007). The thick-skinned Sierra Pampeanas is characterized by basement-cored uplifts of mafic-ultra mafic metamorphic rocks of the Grenvillian Cuyania Terrane to the west (the Sierra Pie de Palo), and to the east, Neoproterozoic – Early Paleozoic felsic metamorphic rocks of the Pampia Terrane, with sedimentary basins located between the uplifts (e.g. Ramos et al., 2002; Vujovich et al., 2004; Alvarado et al., 2007, 2009; Pfiffner, 2017; Linkimer et al., 2020). The Precordillera is a thin-skinned fold and thrust belt composed of Paleozoic sedimentary rocks underlain by the Cuyania Terrane (e.g., Ramos et al., 1996; Ramos et al., 2002; Levina et al., 2014; Pfiffner, 2017; Linkimer et al., 2020). To the west of the Precordillera is the Iglesia basin (North) and Calingasta basin (South) followed by the high Andes (the Principal Cordillera and the Frontal Cordillera). The Principal Cordillera is composed of Mesozoic to Cenozoic sedimentary and volcanic rocks. The Frontal Cordillera is composed of Paleozoic to Mesozoic volcanic rocks and includes the Cuyania and Chilienia Terranes. Both are characterized by thick- and thin-skinned thrust belts (e.g., Ramos et al., 1996; Ramos et al., 2002; Martínez et al., 2015; Pfiffner, 2017; Capaldi et al., 2020). Further east of the Sierra Pampeanas is the Rio de la Plata Craton which is composed of Precambrian to Early Paleozoic metamorphic rocks (Pfiffner, 2017).

The crust above the flat slab decreases in thickness from west to east. It can be as thick as ~70 km beneath the high Andes, ~50 km beneath the western Sierras Pampeanas, and thins to ~35 km beneath the eastern Sierra Pampeanas (Gilbert et al., 2006; Gans et al., 2011; Porter et al., 2012; Richardson et al., 2012; Ammirati et al., 2015; Linkimer et al., 2020). The root of the Rio de la Plata craton may be sufficiently deep to have inhibited the eastern advancement of the flat slab (Booker et al., 2004). This overthickened crust, in conjunction with evidence of eclogitization of the lower crust in the Cuyania Terrane (Alvarado et al., 2007; 2009; Marot et al., 2014; Ammirati et al., 2015; Pfiffner, 2017, Linkinmer et al., 2020), provide support for hypotheses of lithospheric root formation in the vicinity of the flat slab. Several studies have suggested episodic lithospheric removal north of the Pampean flat slab (e.g., Kay & Kay, 1993; Beck & Zandt, 2002; Bianchi et al., 2013; Ducea et al., 2013; Wang et al., 2015; Beck et al., 2015) which multiple investigators have attributed to Rayleigh-Taylor instability (e.g., DeCelles et al., 2015; Schoenbohm et al., 2015; Murray et al., 2015). The western Sierras Pampeanas has high rates of crustal seismicity and a long history of damaging earthquakes, including the 1944 event that damaged much of the city of San Juan (Alvarado and Beck, 2006; Alvarado et al., 2009; Linkimer, 2011; Venerdini et al., 2020; Linkimer et al., 2020).

The Juan Fernandez Ridge is a ~30 km wide and ~800 km long chain of seamounts, guyots, and islands trending roughly East-West that intersects the Peru-Chile trench off the western coast of South America at ~33.4°S (e.g., von Huene et al., 1997; Rodrigo & Lara, 2014; Lara et al., 2018). It was created at the Juan Fernandez hotspot and has been progressively migrating southward relative to South America over time (Yáñez et al., 2001, 2002; Bello-González et al., 2018; Lara et al., 2018). The positive buoyancy of the JFR and its spatial correlation with the Pampean flat slab suggest a genetic relation between the two (e.g., Ramos et al., 2002), although while it is a contributing factor to the maintenance of slab

flattening, appears to be not large enough have initiated it (van Hunen et al. 2002; Martinod et al., 2005; Espurt et al. 2008; Manea et al., 2017; Linkimer et al., 2020). Bello-González et al. (2018) suggest that the younger and hence more buoyant Copiapó and Taltal Ridges, located north of the JFR, may have contributed to this flattening as well. These ridges are inferred to be responsible for the La Puna flat slab that initiated 18 Ma and returned to normal subduction 12 Ma after their southward migration. The subduction of the JFR also appears to have acted as a barrier to large earthquakes such as the M_S = 7.9 1943 earthquake (Contreras-Reyes & Carrizo; 2011) and more recently delimited both the northward propagation of the M8.8 2010 Maule earthquake and the southern propagation of the M8.3 2015 Illapel earthquake (e.g., Tilmann et al., 2015; Comte et al., 2019).

3 Data and Processing

As part of a broader effort to provide better constraints on the dynamics of flat slab subduction, we generated more comprehensive catalogues than currently exist for local earthquakes recorded by several temporary broadband seismic deployments in the Pampean flat slab region. Principal among these are the 40 station Sierras Pampeanas Experiment using a Multicomponent BRoadband Array (SIEMBRA) (Beck & Zandt, 2007) and the 12 station Eastern Sierra Pampeanas (ESP) (Gilbert, 2008) temporary broad-band deployments, both of which are located in Argentina above the Pampean flat slab (Figure 1b). SIEMBRA was installed in late 2007 and recorded continuously for almost 2 years. ESP started later (August, 2008) and continued recording for several months after SIEMBRA was demobilized. While we considered the entirety of the SIEMBRA dataset, the limited aperture and coverage of ESP on its own makes it less useful for this study, and so we examined only the 16 months of the ESP dataset that overlapped with SIEMBRA. Moreover, while the focus of this study is on SIEMBRA/ESP, in order to provide some additional context in the larger subduction regime we also analyzed data recorded by the CHile ARgentina Seismological Measurement Experiment (CHARSME) network that operated from November 2002 to February 2003 with 29 broadband stations and the CHile-ARgentina Geophysical Experiment (CHARGE) network that operated from December 2000 to May 2002 with 23 broadband stations.

The high rate of seismicity recorded by SIEMBRA, on the order of hundreds of detectable events per day, makes the manual generation of a comprehensive catalogue challenging. Hence, we applied an automated algorithm, the Regressive ESTimator (REST) (Comte et al., 2019) to this dataset. REST uses the autoregressive approach of Pisarenko et al. (1987) and Kushnir et al. (1990) to generate detections and onset estimates of phase arrivals, combined with data windowing procedures suggested by Rawles and Thurber (2016). The functions used to detect signals and generate onset estimates are indifferent to waveform morphology, relying instead on statistical estimates of similarity and predictability between a user defined subset of samples and a representation of background noise. To assist in discriminating probable earthquake related phases, REST enforces a causality condition by quantifying the asymmetry of the estimation function and by requiring the amplitude of the waveform to increase by a certain percentage following the estimated onset. In order to maximize the number of locatable events, REST is designed to be overly inclusive at the initial parts of analysis while iteratively identifying and winnowing false positives at later stages.

A key component of the REST procedure is the specification of arrival time windows based on trial hypocenters that are revised as onset estimates are refined. The trial hypocenters

are determined by a search over a grid consisting of spherical elements spaced at about 5 km that span 28°-31°S, 67°-72°W, and from -5 to 300 km depth. Intragrid locations are computed to the 10 m level by trilinear interpolation of the travel times. Hypocenters that occur outside the grid volume are excluded. Travel times are calculated using a spherical coordinate system eikonal equation solver (Li et al., 2009; Zhang et al., 2012). While accurate travel times are advantageous for estimating hypocenters, their use in onset estimation is primarily to center the window in which a phase arrives. Hence, neither the location technique nor the particular wavespeed model used to calculate travel times is critical to the success of the procedure. Mostly for reasons of efficiency, we adopted a 1D wavespeed model (Figure 2) based on the results of other studies in and near this region (Marot et al., 2014) to calculate travel times.

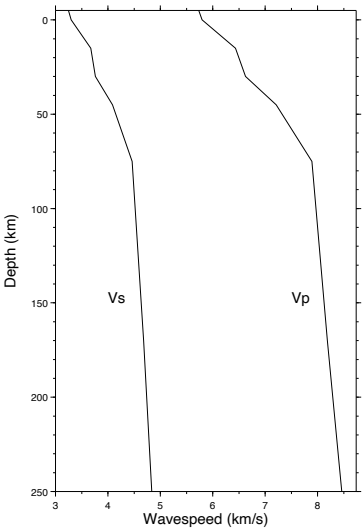

Figure 2. One-dimensional S (left) and P (right) wavespeed models used for calculating travel times used in REST onset estimation and hypocenter location.

The initial processing of the combined SIEMBRA/ESP dataset by REST resulted in 143,716 probable hypocenters with 3,312,422 P and 2,556,506 S onset estimates. Many of these locations, however, are not well constrained due to combinations of poor recording station geometry and potential arrival time outliers. For purposes of this study, we confine our attention to those hypocenters that pass restrictive quality criteria: specifically, we require a standard deviation of residuals less than 0.5 s, a minimum number of 12 phases reporting with at least 3 of those being S waves, and an estimation of total location uncertainty derived from marginal probability density functions (MPDFs) being less than 10 km. As a result of applying these criteria, the original catalogue was pared down to the 35,924 events with 1,150,786 P arrivals and 1,117,921 S arrivals that are discussed here.

3.1 Assessing Onset Estimation Quality and Hypocenter Accuracy

As the inferences we derive from this study depend primarily on the spatial distribution of hypocenters, we take steps to assess their accuracy. Hypocenter accuracy depends on a combination of network geometry and the precision of both observed arrival times and calculated travel times. The total effect arguably is best appraised by calculating probability density functions (PDFs, e.g., Tarantola & Valette, 1982), and these require estimates of the uncertainties in both observed and calculated times, including the potential for outliers in the dataset. As discussed below, the effects of model related uncertainties can be evaluated by relocating the hypocenters in different wavespeed models, while uncertainties in observations depend largely on how well REST estimates arrival times.

The REST algorithm has been used successfully in other studies involving hypocenter catalogue generation (e.g., Comte et al., 2017, 2019; Lanza et al., 2019; Yarce et al., 2023; Merrill et al., 2022; Littel et al., 2023) but is still a relatively untested procedure and its efficacy has not been extensively documented. In any event, its performance is likely to be somewhat dependent on the specifics of a given dataset. Fortunately, we have available a carefully curated catalogue for SIEMBRA and ESP used in the arrival time tomography study of Linkimer et al. (2020) (referred to hereafter as L2020) consisting of 1092 events with

23,802 P and 24,407 S onset estimates, allowing a direct comparison of manually and automatically generated onset estimates for these networks.

3.1.1 Completeness of the catalogue

As the emphasis of the L2020 study was more on tomography than catalogue completeness, it is not surprising that an automated algorithm would recover many more hypocenters than would manual picking (in this case with an assist from an STA/LTA detector). The estimated magnitude threshold for the 35,924 well recorded events in the REST catalogue is M0.6. Nevertheless, despite the large number of events and the inclusive approach of the REST algorithm, 15 of the 1092 L2020 events were not represented in the REST catalog. These missing events occurred within about 90 s of other events in the catalog, and because the current version of REST allows only one detection within a 90 s window, other potential events within the same window were ignored.

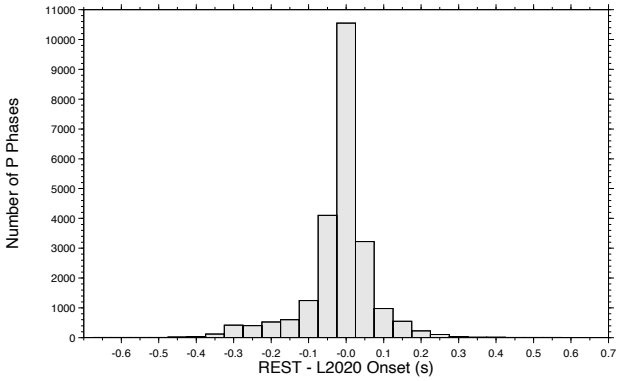

Figure 3. Histogram of differences between REST and L2020 P onset estimates. The L2020 arrival time is subtracted from the REST arrival time after adding 0.05 seconds to account for the phase delay from a forward pass Bessel filter.

3.1.2 Onset estimation accuracy

A few considerations need to be made when comparing onset estimates between manual and automated picks. First, REST currently makes estimates only to the nearest sample. Hence the SIEMBRA 40 Hz sample rate defines an 0.025 s minimum for any potential pick agreement. Second, prior to making an estimate, the raw data is band pass filtered between 1 and 10 Hz with a single pass Bessel filter. This step is taken partly to maximize the energy within the normal local earthquake spectra (variations in the background outside of this spectral band are of no interest and would only introduce false positives), but also to mitigate acausal effects of digital filtering, which are known to occur near the Nyquist frequency (20 Hz for SIEMBRA). The choice of a single (forward) pass Bessel filter is made for the same reason, although a consequence of a single pass in this case results in a systematic delay of about 0.05 s. While an additional pass reversing the filter would undo this delay, it can also generate a low frequency acausal signal. Because the same filter is applied to all seismograms, it does not affect the precision of the pick and the resultant systematic delay is absorbed into the estimate of event origin time. Finally, the emphasis on the lower end of the earthquake spectrum could result in earlier onset estimates resulting from media induced

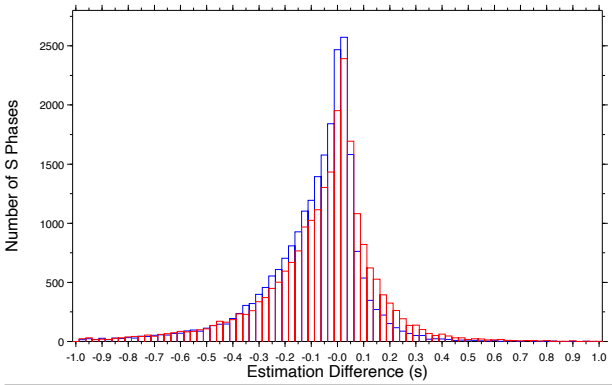

Figure 4. Histogram of differences between REST and L2020 S onset estimates. The L2020 arrival time is subtracted from the REST arrival time after adding 0.05 seconds to account for the phase delay from a forward pass Bessel filter. Blue histogram shows the difference between the L2020 and REST 2C (two horizontal component) estimates, red histogram the difference between the L2020 and REST T (transverse component) estimates.

dispersion, as longer wavelengths will have more opportunities to encounter faster wavespeeds.

To first order, a comparison of P onset estimates for the two catalogues (Figure 3), after correcting for the 0.05 s filter delay, follows a normal distribution, with agreement at a nominal ±0.1 s at a 2σ level of uncertainty. Visual inspection of these arrivals suggests that this level of uncertainty is representative of the intrinsic uncertainty in the picks themselves, meaning that the agreement is arguably as good as one could reasonably expect. In fact, nearly half (45%) of these differences lie within the central bin at ±0.025 s, meaning they are picked at essentially the same sample, and 77% are within in the adjacent two bins or less than 2 samples. At the same time, the distribution appears slightly skewed to negative values, meaning that the REST picks for less certain arrivals tend to be earlier than the manual picks. This is not surprising, since, given the limited dynamic range of human vision, the estimation function generally performs much better than an analyst at both detecting the onset of emergent signals and discriminating them from background noise.

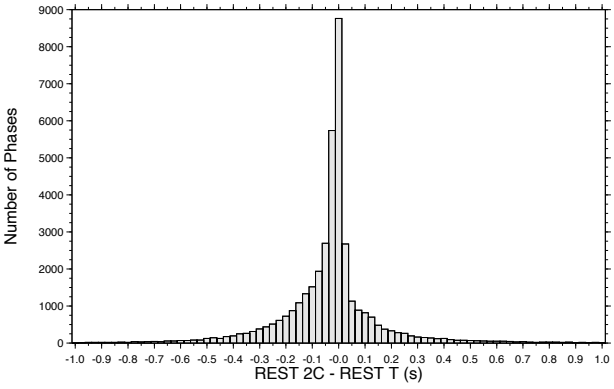

Figure 5. Histogram of differences between REST 2C (two horizontal component) REST T (transverse component) S onset estimates.

Differences in S wave estimates (Figure 4) also approximate a normal distribution, although with a significantly higher level of uncertainty (on the order of ±0.4 s) and skew to negative values (i.e., earlier REST picks). Because many S onsets are obscured by P coda, neither of these results is particularly surprising. At the same time, while REST nominally picks S arrivals by simultaneous regression to both horizontal components, L2020 rotated the horizontals and picked S waves from the transverse (T or SH) component. A motivation for using the T component is to prevent mistakenly picking potential Sp conversions that would arrive before the main S phase. REST can estimate an onset from a T component a posteriori from a known hypocenter, and we generated those estimates to compare with both the L2020 estimates and the original two-component (2C) estimates. The results (red histogram in Figure 4) show that, indeed, the distribution of onset differences is more symmetric when the REST T component is used, while the difference between the T component and 2C REST estimates (Figure 5) is still skewed slightly negative. This suggests that the 2C picks are in some cases picking Sp conversions, and the

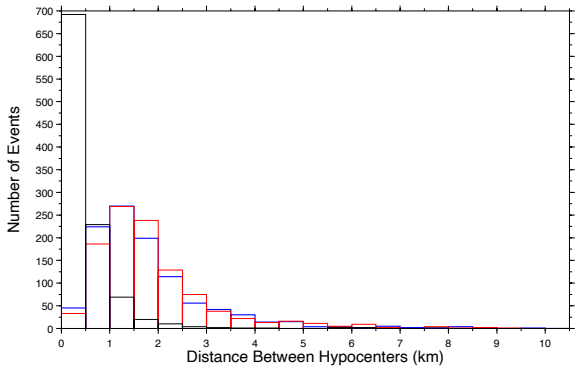

Figure 6. Histogram of distances between hypocenters located in the 1D model shown in Figure 2 using different P and S arrival time estimates. Red and blue histograms compare REST and L2020 locations; red uses REST 2C (two horizontal component) and blue REST T (transverse component) S onset estimates. Black histogram shows the difference in the REST catalogue from using the 2C and T estimates.

time differences (generally less than 0.4 s) suggest that any such conversion is taking place less than about 1 km from the station, as might be expected for stations located on low wavespeed sediments.

3.1.3 Effects of Onset estimation on Hypocenter Location

While automated onset estimation accuracy is of intrinsic interest, for the present study our main concern is its effect on hypocenter location. A comparison of locations (Figure 6) using the L2020, REST 2C, and REST T onset estimates shows that the differences between REST 2C and REST T locations are less than 2 km and 4 km for 90% and 99%, respectively, of the events. The differences between the L2020 and REST (red and blue histograms in Figure 6) are less than 2 km and 4 km for 70% and 94%, respectively, regardless of whether 2C or T components were used. We infer that while T component estimates are likely to be more representative of an actual S arrival time, they appear to have negligible impact on hypocenter uncertainties (at least in comparison to other factors). Moreover, since the differences in S arrival time estimate most likely are due to near surface heterogeneity, their effects on arrival time tomography and related studies would likely be absorbed by station corrections or perturbations to near-surface structure.

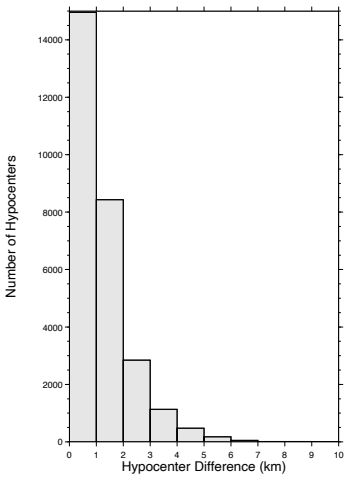

Figure 7. Histogram of distances between hypocenters located in the 1D model shown in Figure 2 and the 3D model of Comte et al. (2017) for the selective catalogue of events.

3.1.4 Effects of Travel Time Computation on Hypocenter Location

To assess the effects of uncertainties in travel time computation on hypocenter locations, we compared locations in the 1D model used to generate onset estimates with those in two 3D wavespeed models: one from L2020 and a second from Comte et al. (2017). Beyond simple changes in absolute location, comparing results in different wavespeed models can illuminate instances where concentrations of hypocenters may result from large gradients in wavespeed. A comparison of results for the Comte et al. (2017) model (Figure 7) show that, after correcting for a systematic bias (1.8 km in longitude, 0.8 km in latitude, and 1.4 km in depth) 83% of the hypocenters are within 2 km of each other and 98% are within 4 km of each other. Results from the L2020 model are similar. These differences are much smaller than the scale of the features that we interpret in this study. Moveover, we detected are no discernable artifacts due to gradient-induced concentrations in either model.

3.1.5 Effects of Double Differencing

Several studies (e.g., Waldhauser and Ellsworth, 2000) have demonstrated that locating events using relative rather than absolute arrival times can improve hypocenter precision by (1) taking direct advantage of the increased precision of relative times estimated from cross-correlated waveforms and/or (2) eliminating the effects of poorly constrained wavespeeds common to ray paths from a group of events recorded at the same station. The first advantage does not apply to this absolute arrival time data set (we note that an initial attempt to generate cross-correlated times was plagued by cycle skips due to waveform complexity), and the second one generally does not generate significant differences in hypocenters when the events are well recorded (e.g., Yarce et al., 2023). Nevertheless, to quantify any potential benefits that might accrue from double differencing, we used the demeaning algorithm described in Roecker et al. (2021) to relocate subsets of events in various parts of the seismic zone defined by the selective catalogue that have significant bearing on our interpretations. Specifically, we differenced arrival times for 5445 crustal depth (< 70 km) hypocenters located in a region of high activity ~31°-32°S, and for 4048 deeper (> 70 km depth) events located in lineaments trending at 20° within the subducted Nazca plate discussed in section 4. Histograms of differences in location (Figure 8a) show that percentages of hypocenters within 1 and 2 km of their original locations are 75% and 91%, respectively, for crustal events, and 65% and 89%, respectively, for the deeper events. A map view comparing locations of the crustal events (Figure 8b) confirms that these differences are of little consequence at the scale length of the features we describe here.

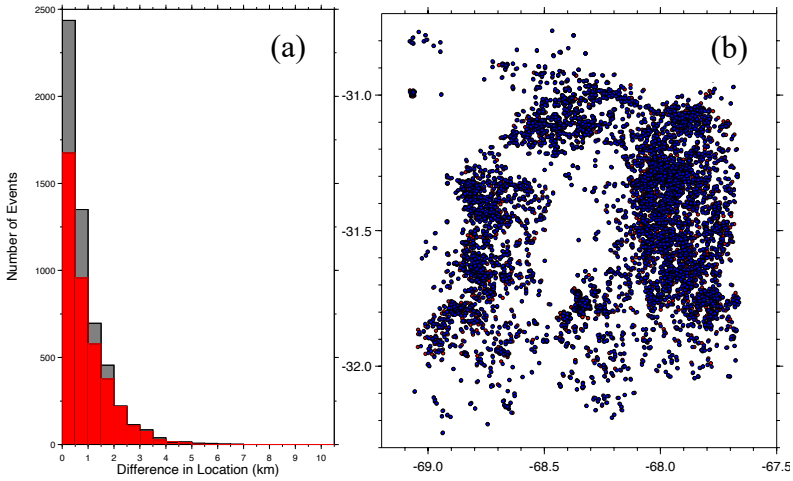

Figure 8. Summary of double differencing results. (a) Histogram of differences between original and differenced hypocenter locations. Black and red histograms bin differences for 5445 hypocenters at crustal depth (< 70 km) and for 4048 hypocenters (> 70 km depth) events located in four of the lineaments in the Nazca plate, respectively. (b) Map of the crustal depth events comparing original locations (closed red circles) and differenced locations (blue circles). Blue circles plot on top of red circles where they overlap. Lines are drawn between original and differenced locations but are mostly obscured in this figure because the differences in location are generally less than the symbol size.

4 Hypocenter Distributions

Most of the patterns in the seismic zone defined by the selective SIEMBRA/ESP catalogue can be illustrated satisfactorily with traditional two-dimensional cross sections and map projections. Nevertheless, some, like the relationships between shallow and deep hypocenters, are more easily viewed in a three-dimensional rendering, available in the

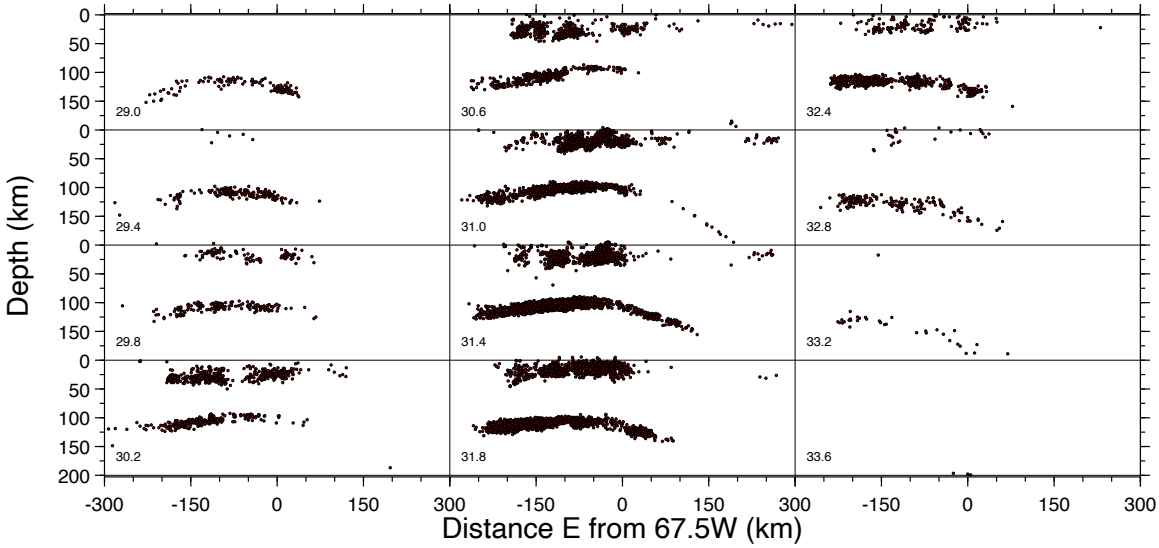

Figure 9. Latitudinal (W-E) cross sections of the hypocenters in the REST catalog. Each section is centered at 67.5°W and includes hypocenters within ±20 km of the latitude shown at the lower left corner of each panel. Note the correspondence between shallow and deep events associated with the dense activity of the JFRC in panels in the central panels. The gap in shallow seismicity between SIEMBRA and ESP is evident in these central panels as well.

supplementary material, that permits arbitrary perspectives[1].

Several first order features evident in the distribution of hypocenters have been described in previous studies (e.g., Anderson et al., 2007; Alvarado et al., 2009; Linkimer et al., 2020). First, seismic activity is concentrated in two distinct depth intervals (see cross sections in Figures 9 and 10): one in the upper ~50 km that presumably is located within the crust of South America, and the other at depths greater than ~80 km that presumably occurs within the subducted Nazca plate. The intervening South American upper mantle is virtually aseismic. Second, while ostensibly "flat", the events in the subducted Nazca plate define quazi-arcuate (concave-down) features both latitudinally (e.g., the EW section at 31.4°S in Figure 9) and longitudinally (e.g., the NS section at 67.4°W in Figure 10). Finally, the events within the shallowest part of the subducted Nazca plate (map view of deeper events in Figure 11b) lie within an exceptionally active region between about 31°-32°S, that, given its location and bearing of about 70°, has been interpreted to be the subducted extension of the JFR (Figure 1). Below, we refer the events located in this region as the "JFR Concentration" or JFRC.

While corroboration of previously recognized features bolsters confidence in the current catalog, other previously unrecognized patterns in seismicity emerge as well. Principal among these is a series of parallel lineaments in the subducted Nazca plate (Figure 11b). There appear to be at least four of these lineaments that trend at about 20° east of north and are separated from each other by about 50 km. Each of these lineaments intersect the JFRC; the westernmost appear to be continuous though the JFRC, while those in the east appear to be confined to the south of it.

[1] For now this will be the following link to a file on Google Drive. Download the file and open in any browser. https://drive.google.com/file/d/1CDMMpeudRDSCmae3Z35fTdnW5euoAgBF/view?usp=share_link

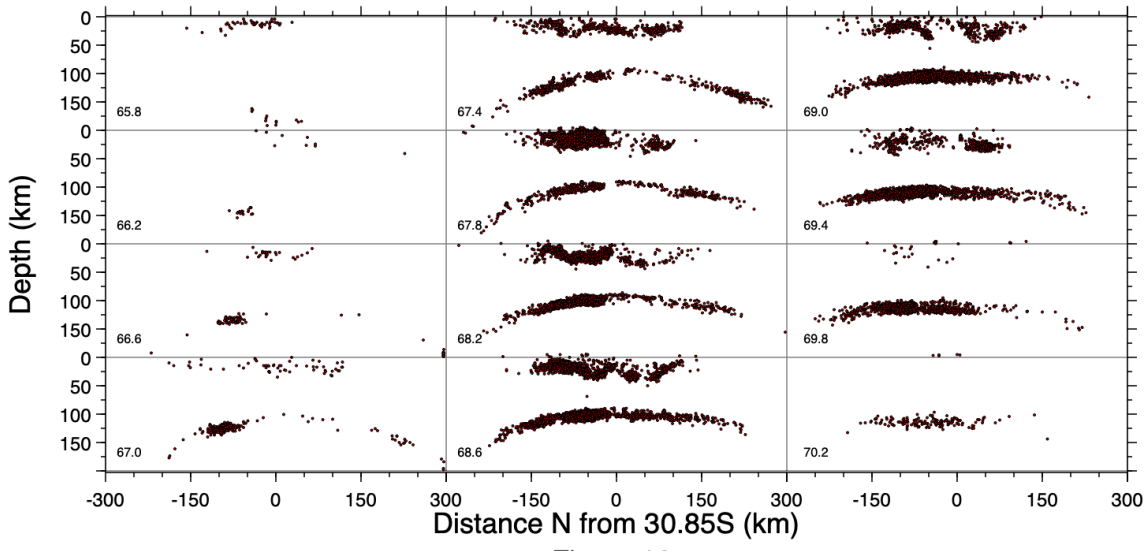

513

Figure 10. Longitudinal (N-S) cross sections of the hypocenters in the REST catalog. Each section is centered at 30.85°S and includes hypocenters within ±20 km of the longitude shown at the lower left corner of each panel except for the upper left panel which includes all hypocenters east of 66.4°W. Note the correspondence between shallow and deep events associated with the dense activity of the JFRC in panels at 68.2°W and 67.8°W. Also, the easternmost parallel ridges to the south of the JFRC is clearly visible in the cluster of activity in the four left-most panels.

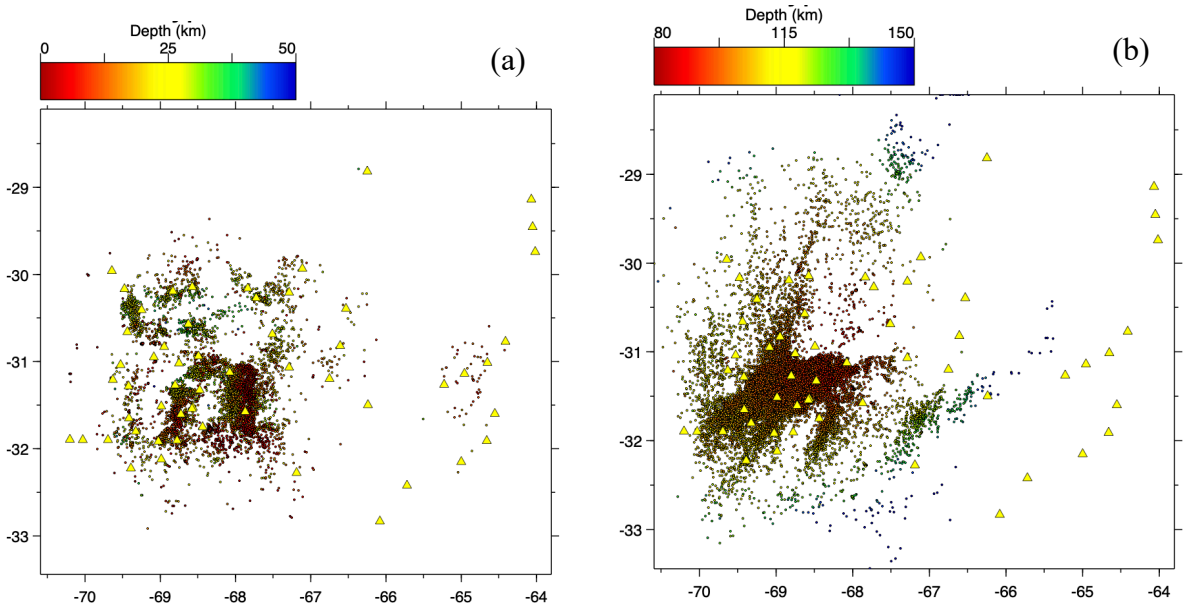

Figure 11. Map views of events with in the (a) upper (crustal) seismic zone (< 50 km depth) and (b) deeper (Nazca) seismic zone (> 70 km depth). Hypocenters are plotted as closed circles with colors corresponding to depth as indicated in the palette near the top of the figure. Yellow triangles locate the stations of the SIEMBRA/ESP network.

514 Seismicity at crustal depths (< 50 km; Figure 11a), while scattered as may be expected in
515 a region of active continental shortening, nevertheless is highly concentrated in an "inverted
516 U" pattern between 31°-32°S and 67.5°-69°W. There is a peak in the level of activity between
517 about 20-24 km depth (i.e., mid-crust, Figure 12), nevertheless there are several thousand
518 events (3832, or about half of all crustal seismicity) located between 20-40 km depth (i.e., the

mid to lower crust for this region). The gradients in levels of activity inside and outside of this region are remarkably sharp, with few if any events found in the crust between the SEIMBRA and ESP networks, despite the presence of apparently active faults in this region associated with shortening in the Pampean fold-thrust belt (Figure 11a). This region is well within the aperture of these networks and reasonably close to stations in both; hence this lack of events is unlikely to be due to station geometry.

Perhaps even more remarkable is a strong spatial correlation between this "inverted U" region of intense seismicity in crust with a similar feature 50 km beneath it in the subducted Nazca plate (Figure 11b). While the correlation between seismic activity in the deep and shallow regions can be discerned from a simple plot of hypocenters (Figures 11 a and b), the relative intensity of activity is obscured by the large number of events in this region. A more meaningful view may be obtained from contours of "earthquake intensity" by summing up the number of events, weighted by their respective magnitudes, in volumetric bins. While moments would be more directly representative of energy release, we choose to sum magnitudes (or log moments) for two reasons: first, a representation by moments will be dominated by a few of the larger events that are statistical outliers for a short duration deployment, and second, we use a simple amplitude/distance relationship to calculate M_L, and the associated uncertainties using these for moment estimation (as an exponential of magnitude) would make such a rendering practically useless. Note that the intensity plot for the deeper events (Figure 13b) appears to reveal some internal structure in the JFRC around 31.4°S, 69.1°W with the same 20° trend as the lineaments, emphasizing the close relationship between the two.

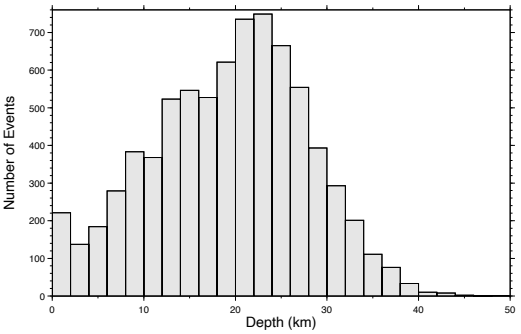

Figure 12. Histogram of earthquake depths within the crust.

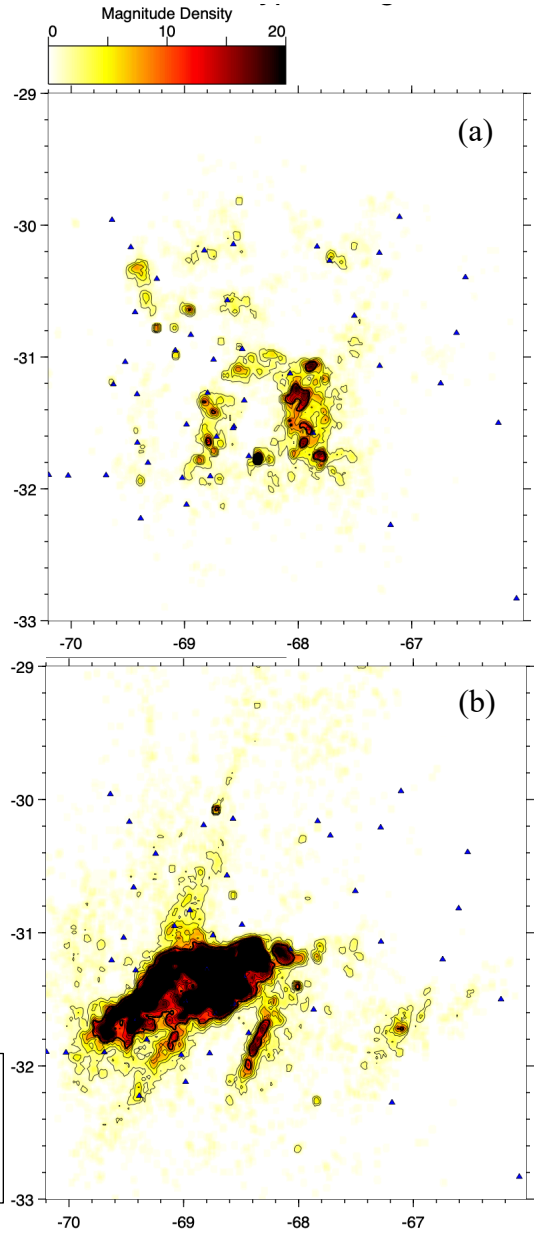

Figure 13. Maps of earthquake magnitude density for (a) Shallow events and (b) Deep Events. Blue Triangles locate seismic stations. Units are arbitrary but the palette is pegged at 20 to clarify variations in density within the JFRC in (b).

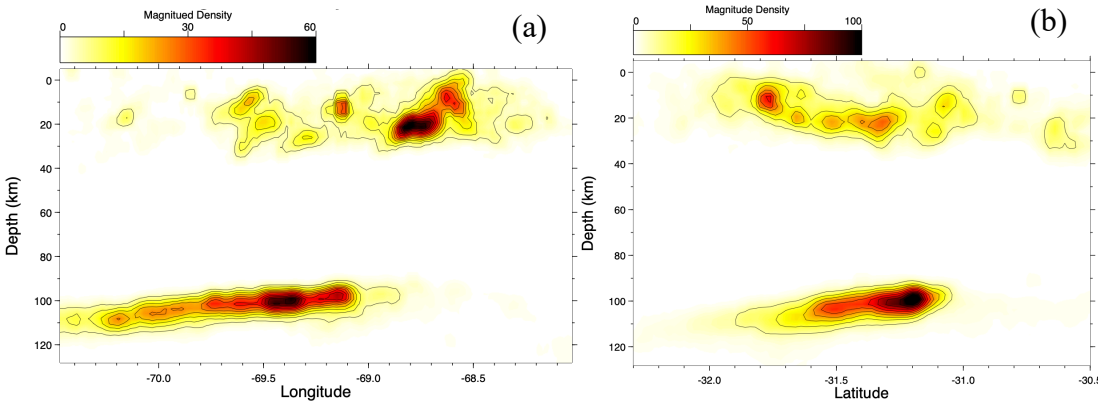

Figure 14. Cross-sections of magnitude density for events in the vicinity of the JFRC. (a) EW cross-section for events between 30.90°S and 32.30°S. Note apparent dip to the west of shallow features. (b) NS cross-section for events between 67.25°W and 69.70°W. Units are arbitrary but densities for deeper events are scaled by a factor of 1/6 to normalize with those for shallow events.

While the decline in seismicity south of 32°S could be partially attributed to the southern limit of the SIEMBRA deployment, the gradient in activity level (Figures 11, 13, and 14) is still steep. The sudden decrease in seismicity rate to the north of 31°S occurs right in the middle of the network and hence cannot be an artifact of recording geometry. This substantial gradient occurs directly above a similar gradient in the deeper JFRC. Other features, such as the "inverted U" shape of the high-rate regions, are also present in the JFRC, although displaced about 50 km to the east (Figures 13 and 14). Viewed in cross section, the crustal seismicity in this "inverted U" appears to define features that dip ~45° to the west (Figure 14a), the easternmost of which project down to the eastern termination of the JFRC.

5 Focal Mechanisms

REST can also be used to estimate first motion polarities based on the P arrival times. To do so, REST samples a user-specified window before the onset to provide a noise estimate, and then progresses after the onset until a zero-crossing (defined as the point that has the same amplitude as the start point) is encountered to create a polarity window. An SNR estimate, used as a metric for quality, is made from the maximum amplitude in the polarity window divided by the noise estimate. Following Comte et al. (2019), these polarities are converted to impulsive and emergent arrivals based on the SNR ratio and used as input to the FOCMECH routine of Snoke et al. (2003) to generate focal mechanisms. A total of 12,172 mechanisms were obtained for the 35,924 events in the selected catalog, most of which (10,819) are located in the deeper seismic (Nazca) zone. Of these, we focus on those mechanisms that were generated by, and are consistent with, with the most observations. The deeper events have 2686 mechanisms constrained by at least 20 polarities, and 156 with at least 36 polarities. The shallower events are less well recorded; nevertheless, there are 156 constrained by at least 18 polarities. These mechanisms are plotted in map and cross section views (Figures 15 and 16). Because of the large number of mechanisms determined we plot the actual mechanisms only for the 156 better constrained; the remainder are represented only by the type of mechanism (normal or reverse as red and blue closed circles, respectively, in Figures 15 and 16).

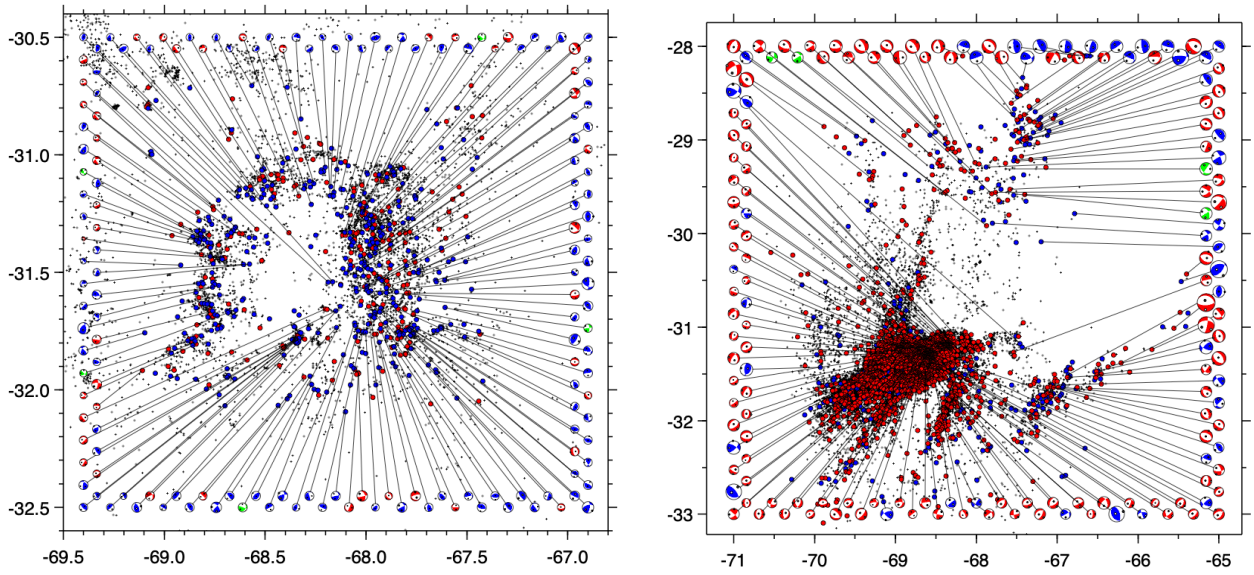

Figure 15. Map view of lower hemisphere focal mechanisms for (*left*) shallow events located above the JFRC and (*right*) deeper events, plotted as blue circles for thrust events, red circles for normal events, and green for strike-slip (near vertical fault plane). 156 mechanisms with more than 18 polarities (shallow) and 36 polarities (deep) are plotted along the perimeter with lines connecting them to their respective hypocenter. Remaining events for which no mechanism could be determined are plotted as small crosses.

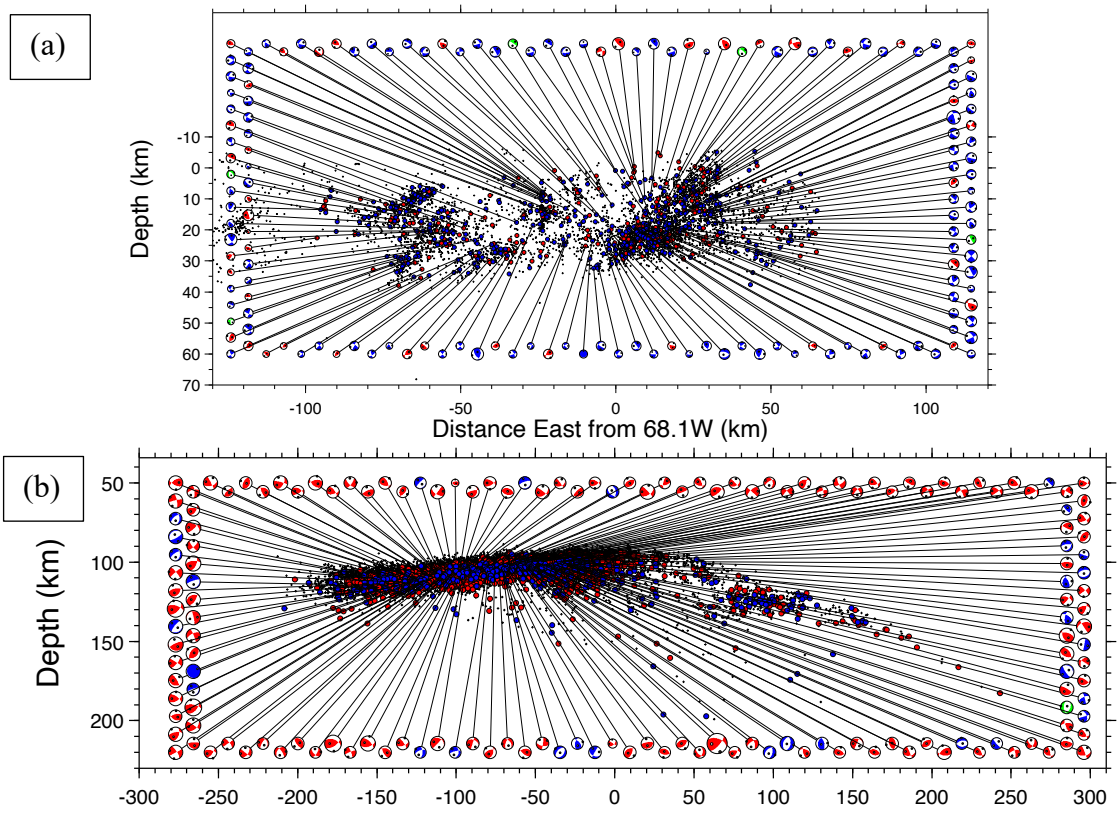

Figure 16. Cross section (EW) of back (northern) hemisphere focal mechanisms for (a) shallow events located above the JFRC and (b) deeper events associated with the JFRC. Symbols are the same as in Figure 15. Note that as there are many more normal mechanisms for the deeper events in (b), the thrust events (blue circles) are plotted on top of them.

While these patterns in these plots of mechanisms are complex, in general thrust mechanisms are more prevalent in the crust (70% of the 156 best mechanisms are thrust) while normal mechanisms overwhelmingly dominate the deeper events: of the 2686 well recorded mechanisms, 2182 (81%) are normal, 427 (16%) are thrust, and the remaining 77 (3%) are strike slip or indeterminant with nearly vertical fault planes.

6 Comparison with Hypocenters from the CHARGE and CHARSME Networks

In addition to SIEMBRA/ESP, two networks for which we have access to continuous seismograms operated in this region: the CHile ARgentina Seismological Measurement Experiment (CHARSME) network (Pardo et al., 2003) that operated from November 2002 to February 2003 with 29 broadband stations and the Chile ARgentina Geophysical Experiment (CHARGE) network (Wagner et al., 2005) that operated from December 2000 to May 2002 with 23 broadband stations. We applied the same processing with REST to these two datasets in order to provide some corroboration for the patterns observed in the SIEMBRA/ESP catalogue, and also to determine how some of these features might extend beyond the aperture of the SIEMBRA/ESP network.

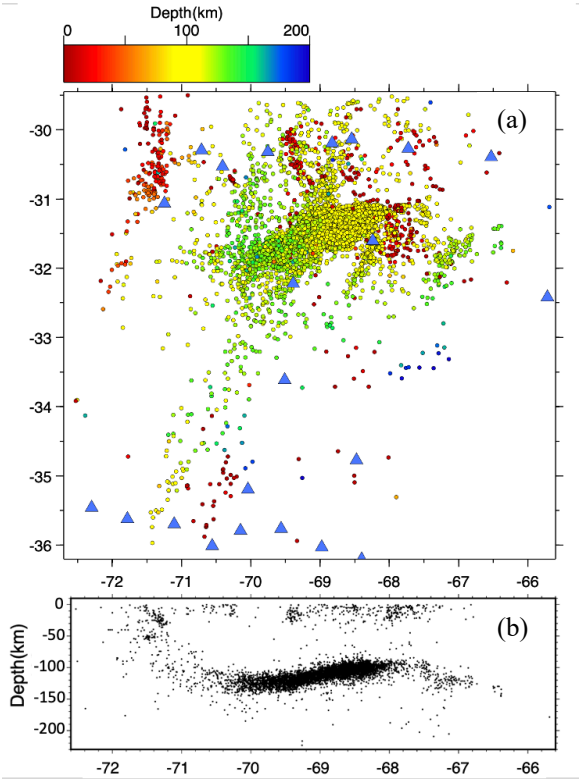

Figure 17. CHARGE hypocenters. (a) Map view of the hypocenters (circles with colors corresponding to depth as indicated in the palette at the top of the figure) and stations (blue triangles) within the bounds of the map. (b) W-E cross-section of all the hypocenters in the dataset.

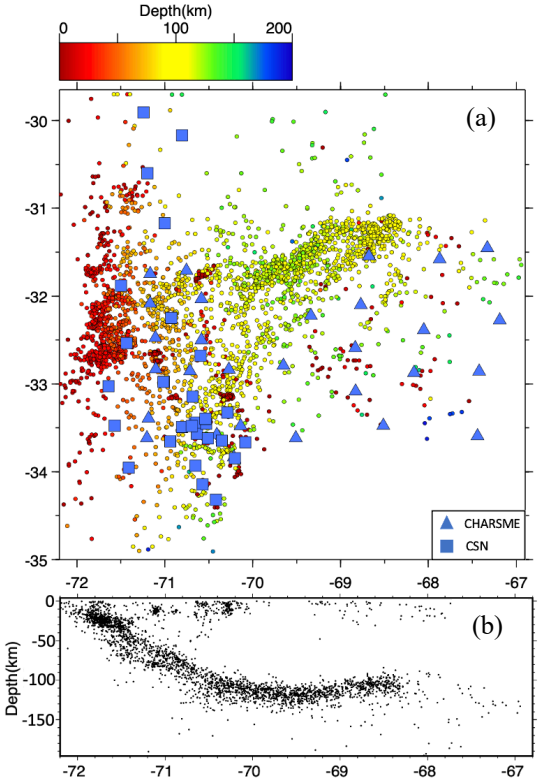

Figure 18. CHARSME/CSN hypocenters. (a) Map view of the hypocenters (circles with colors corresponding to depth as indicated in the palette at the top of the figure) and stations (blue triangles and squares). (b) WE cross-section of all the hypocenters in the dataset.

Application of REST to data from the CHARGE network (Figures 1b and 17) resulted in a catalogue of 14,672 events with 140,663 P arrivals and 115,910 S arrivals. Because this dataset is

considerably smaller than that from SIEMBRA/ESP, we applied a less restrictive criteria in filtering the hypocenters. In this case, an accepted event was required to have a minimum of 10 phases with at least 3 S arrivals, a maximum residual standard deviation of 0.8 seconds, a maximum total uncertainty of 25 km. Application of this criteria resulted in 7,313 events with 76,185 P arrivals and 69,055 S arrivals. Plots of these events (Figure 17) show that, while few crustal depth events could be located and the resolution of deeper features is clearly degraded compared to the SIEMBRA/ESP results, similar trends appear in the deeper seismicity. Specifically, both the JFRC and the four parallel NNE-SSW (20°) trending lineations are evident, along with a ~25 km shallowing of the slab (Figure 17b) beneath the Pampeanas. The larger aperture of this network additionally provides some evidence that the westernmost lineation in deep seismicity extends as far south as 36°S (Figure 17a), although the frequency of activity decreases substantially south of about 32.5°S.

The CHARMSE network is located mostly to the south of the JFRC. Application of REST to data from CHARSME allowed the creation of a catalogue of 8,419 events with 108,771 P arrivals and 95,142 S arrivals. We were able to able to augment this catalogue with manually picked arrivals from about 500 events in the Chilean Seismic Network (CSN) catalogue. The combined catalogue was then filtered with the same criteria applied to the CHARGE dataset, resulting in 3,176 events with 48,658 P arrivals and 45,285 S arrivals. Plots of the filtered locations show the same ~70° trend in the JFRC catalogues (Figure 18a) and shallowing of the slab beneath the Pampeanas (Figure 18b), even though many of these events are outside of the aperture of the CHARMSE network. While there is some suggestion of the westernmost lineation in deep seismicity extending as far south as 36°S the hypocenters from this catalogue unfortunately are too sparse to corroborate any other features in the crust or mantle.

7 Discussion

Several studies have remarked on the correlation between the JFR and the concentration of events we see trending at ~70° (e.g., Smalley & Isacks, 1987; Yañez et al., 2002), strongly suggesting the subduction of this feature as the cause of this dense cluster of activity. This relationship led us to look for similar features on the Nazca plate that might explain the NNE-SSW (20°) lineaments we observe in the deeper seismicity. An inspection of Nazca plate bathymetry (Figure 19; GEBCO Compilation Group, 2022)) shows that at least two major features, the Nazca and Iquique Ridges also trend at about 20°, and although these features are far to the north of the JFR, the JFR may have been parallel to the Nazca and Iquique Ridges during the late Oligocene- early Miocene (Bello-González et al., 2018; Lara et al., 2018). However, this would not explain the 20° lineaments we observe, as these are contemporaneous with the more recent 70° trend of the JFR. Closer inspections of the Nazca plate bathymetry west of the flat slab region (Figure 20), reveals several less prominent ridges trending at 20°. One of these minor ridges intersects the JFR at the Isla Alejandro Selkirk (Figure 21) and shows a remarkably strong correlation with the westernmost lineation in the deeper seismicity.

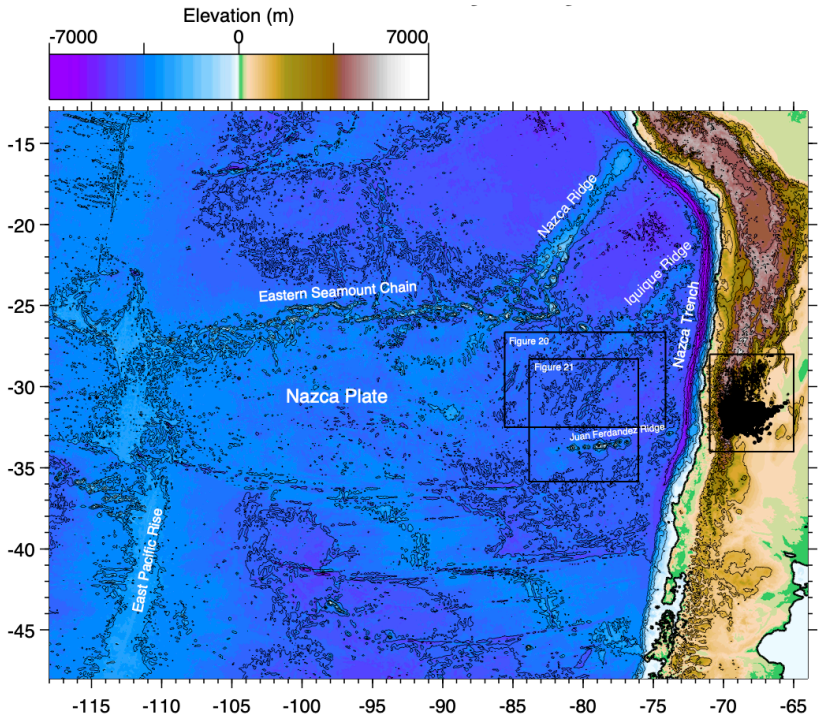

678

Figure 19. The local seismicity in the context of the Nazca plate. Bathymetry and topography are shown in the palette at the top of the figure. Major aseismic ridges (Nazca, Iquique, JFR, and Eastern Seamounts) are labeled. The black rectangle at the far right locates the study area, with the locations of the hypocenters in the refined catalogue plotted as small crosses. The other two rectangles locate the close-ups of bathymetry shown in Figures 20 and 21. Bathymetric data are from the GEBCO Compilation Group (2022).

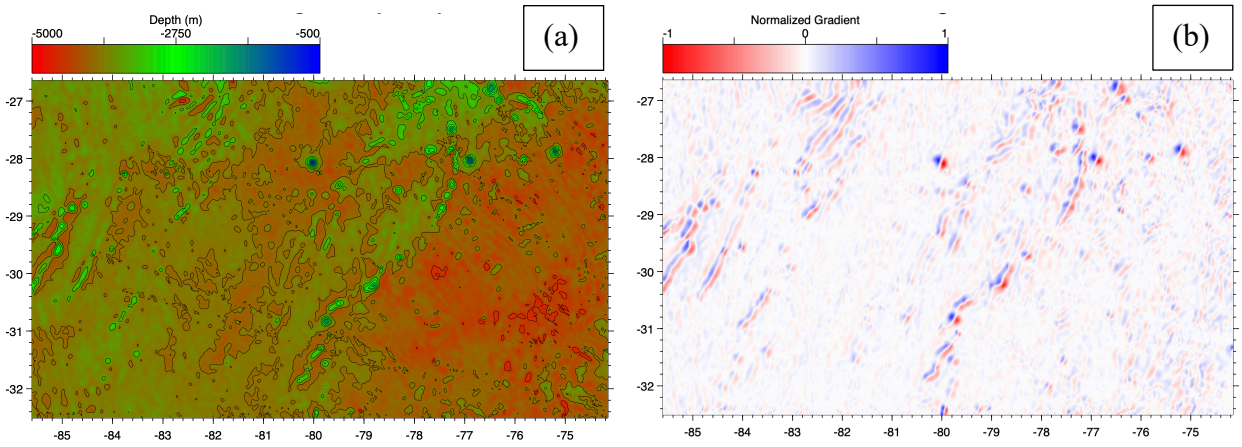

Figure 20. (a) Nazca plate bathymetry north of the JFR within a rectangle, shown in Figure 19, that excludes the more prominent ridges and seamount chains to the north and south. Note the bright green ridge-like features trending NNE. (b) Bathymetric gradients in the same region, obtained by convolving a Prewitt mask rotated by 27° degrees with the bathymetry shown in (a), which illuminates gradients from a source at 117° azimuth. Values are significant only in a relative sense and so are normalized to 1. Blues are positive (front side), red negative (back side) gradients.

679 A causal relationship between subducted bathymetric highs and clustering of seismicity
680 far from the trench suggests that the effects of even relatively minor features can persist in
681 a subduction regime long after they are consumed. While some have argued that small

features are likely to be decapitated and accreted onto the forearc (e.g., Yang et al., 2022), our results suggest that even minor bathymetric highs can remain largely intact, persisting at least some 200 km beyond their initial encounter with the trench. These intact minor ridges could add positive buoyancy to the slab, which would contribute to slab flattening, although the concave down patterns in the longitudinal cross sections of seismicity (Figure 10), suggests these limbs are dipping down and away from the JFR. As noted above, the subduction of bathymetric highs has also been linked to higher rates of subduction erosion (e.g., Hampel et al., 2004; Navarro-Aràngiuz et al., 2022), and in this case the regular spacing between lineaments that are sub-parallel to the trench suggests that such erosion is more likely to be episodic than continuous, as has been suggested both for the "Norte Chico" region of Chile directly to the west of the JFRC (Comte et al., 2019) and for the Puna region to the north of the Pampeanas by Goss et al (2013).

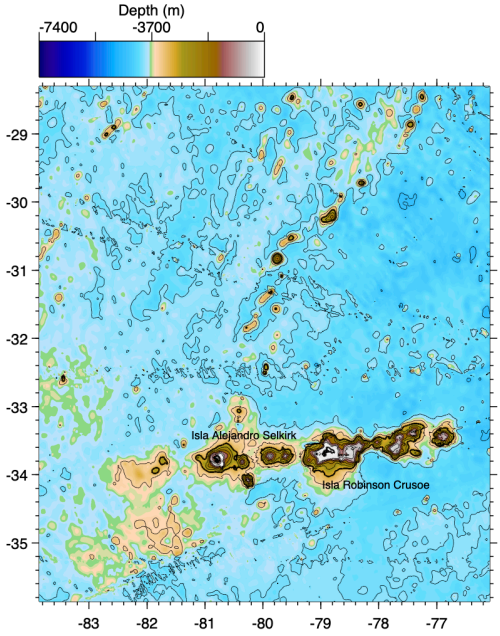

Figure 21. Bathymetry within a rectangle shown in Figure 19 in the vicinity of Isla Alejandro Selkirk. The palette is shifted to emphasize features with depths less than 3700 m located to the N and SW of the island that correlate strongly with the westernmost band of the JSRC shown in Figures 11b and 13b at about 70°W. These features are also likely above the Carbon Compensation Depth. The linear features trending WNW and WSW in this figure are artifacts in the bathymetric data caused by merging ship tracks.

Any genetic relation suggested by the spatial correlation between seismicity in the subducting Nazca plate and the crust directly above it seems unlikely at first because differences in temperature and lithology in the mantle and the crust would lead to different deformation regimes, and the South American upper mantle between the two is virtually aseismic. At the same time, despite the predominance of thrust faulting one would expect from crustal shortening, the geology of the Sierra Pampeanas does not show any clear correlation with the observed trends in seismicity in the mid to lower crust, in particular with the highly intensive "inverted U". Moreover, while a local increase in stress could be associated with subducted bathymetric highs (Scholz & Small, 1997; Contreras-Reyes & Carrizo, 2011), the effects of such stress would tend to diffuse over distances of tens of kilometers, and hence is unlikely to be a causative factor.

The lack of any clear correspondence with surficial geology and the near-vertical nature of the correlation between deep and shallow seismicity suggests that gravity (which defines vertical), in the form of negative buoyancy, plays a fundamental role. We hypothesize that this near-vertical correspondence between the deep and shallow seismicity is a result of subducted bathymetric highs releasing volatiles that travel up through the South American mantle, increasing the pore pressure within and essentially fracking the crust, which in turn activates mid to lower crustal seismicity (Figure 22).

The Nazca plate is believed to be hydrated due to extensive faulting along the outer rise near the JFR (Kopp et al., 2004; Ranero et al., 2005; Fromm et al., 2006). With depth, pressure and temperature (PT) conditions are not favorable for brittle deformation and faulting (e.g., Meade and Jeanloz, 1991). However, seismicity at intermediate depths in flats slabs has been attributed to dehydration reactions (phase changes) and an increase in fluid pressure which results in apparent brittle deformation and reactivation of faults (e.g., Ammirati et al 2015; Zheng et al., 2016). Porter et al. (2012) suggested that the PT conditions in the mantle of the Pampean flat slab cause dehydration of serpentinite and seismicity related to dehydration embrittlement in the oceanic mantle, in agreement with inferences from other studies (Gans et al., 2011; Marot et al 2014; Linkimer et al., 2020). Dehydration of serpentinite has also been linked to the lower plane of double seismic zones (Hacker et al. 2003b). Normal faulting mechanisms dominate the lower plane of the double seismic zone beneath Chile in the JFR region (e.g., Marot et al., 2013) and, as shown here, in the JFRC as well. At the same time, Ammirati et al. (2015) postulate that slab seismicity is related to dehydration of the oceanic crust rather than the mantle. In either case, serpentinite is stable at temperatures less than 680°C and pressures less than 6.5 GPa (Zheng et al., 2016). Temperatures in the Pampean flat slab are likely less than 600°C, which promotes retention of water to intermediate depths (Marot et al., 2014; Manea et al., 2017). As pressure and temperature increases, the stability of serpentinite decreases, which promotes dehydration (Zheng et al., 2016). There is evidence of serpentinized mantle in the region above the flat slab as seen in low seismic velocities and high Vp/Vs ratios (Porter et al., 2012; Marot et al., 2014; Linkimer et al., 2020) and at the base of the South American plate where the Nazca Plate subducts under Chile as seen in a strong anisotropic signal (Nikulin et al., 2019). Progressive dehydration of the flat slab from west to east has been suggested by multiple studies (Wagner et al., 2006; 2008; Porter et al., 2012; Marot et al., 2014; Ammirati et al., 2015; Linkimer et al., 2020) and has been postulated to be related to the permeability of the slab changing with the transition from normal to flat subduction (Porter et al., 2012) or to migration of water deeper into the slab which is released later on (Linkimer et al., 2020).

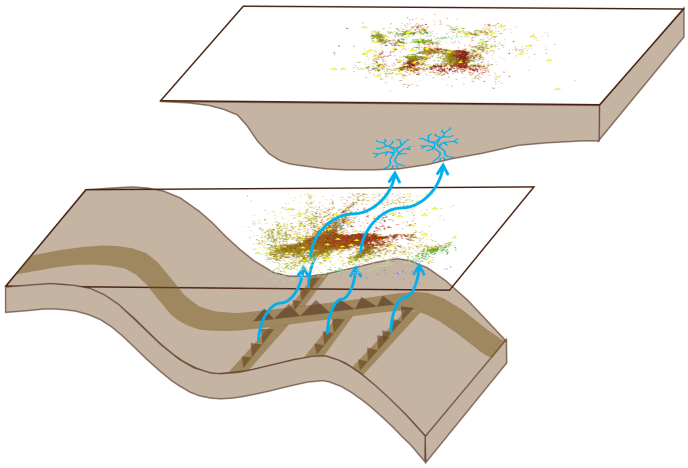

Figure 22. A conceptual diagram of volatiles being released from seamounts on the subducting oceanic slab and creating seismicity in the slab, which ascend into the continental crust and create seismicity through increased pore pressure (i.e., "fracking").

The trends observed in this study are specifically related to the bathymetric highs of the plate and not to the entire subducting oceanic lithosphere, suggesting that there is some characteristic of these features that promotes devolatilization reactions more than "normal" oceanic crust or lithosphere. A possible explanation is that seamounts have been associated with transporting large amounts of fluid into the subduction channel compared to smoother oceanic lithosphere, increasing dehydration reactions and fluid release within the subduction channel (e.g., Ellis et al., 2015; Pommier & Evans 2017; Chesley et al., 2021).

An alternative explanation that may more easily account for these trends in seismicity is the release of carbon dioxide due to decarbonation (e.g., Miller et al., 2004; Famin et al., 2008; Gunatilake & Miller, 2022) as bathymetric highs spend more time above the carbonate compensation depth (CCD) prior to subduction and hence would be capable of accumulating more biogenic carbonate than the surrounding sea floor. The seamounts of the JFR are between heights of 1,000 m above sea level to 500m below sea level with a common base at 3,900m depth (Rodrigo & Lara, 2014; Lara et al., 2018) and the CCD is ~4,500 m (Hebbeln et al., 2000). Additionally, the minor ridges in our region of study are well above 4,500 m depth (Figure 20) and studies in this region provide evidence of carbonates on the ridges of the Nazca Plate (e.g., Hebbeln et al., 2000; Paul et al., 2019; Devey et al., 2021). Perkins et al. (2006) show that carbonates can persist to depths of 100-200 km in a flat slab subduction zone, supporting the inference that subducted carbonates can be a source for decarbonation in the region. We also note that carbonated melts have been found in the JFR (Devey et al., 2000) and in other regions of the Nazca Plate (Villagómez et al., 2014). Carbonated melts transport carbon from the mantle to the crust over a wide range of temperatures (Jones et al., 2013). Decarbonation could also explain the predominance of extensional focal mechanisms in the Nazca slab as a relatively larger space (that may be created by extension) is required for the release of carbon dioxide compared to water. Decarbonation has also been suggested to be responsible for the aftershock sequence of the 2014 Iquique earthquake in Chile (Gunatilake & Miller, 2022). Furthermore, a magnetotelluric study done by Burd et al. (2013) showed regions of low resistivity in the South American plate which correlate with hypocenter locations we observe at shallower depths. There is also a region of low resistivity beneath the Sierras de Córdoba (Booker et al., 2004) that coincides with a low velocity zone which Porter et al. (2012) suggest occurs due to the release of fluids from the slab as it resumes normal subduction. These low resistivity zones could be due to the presence of water, but the connectivity required to lower resistivity is uncertain. Low resistivity can also be caused by graphite, which has been postulated to form in the subducting and overriding plate through decarbonation of subducted carbonates (Galvez et al., 2013) and carbonated melts (Selway, 2014) in reducing conditions.

An important question to address is: How would volatiles travel from the subducting slab to the upper crust? Several studies have inferred the presence of structures that could act as conduits for fluid migration from the subducting plate to the overlying crust. For example, Farías et al. (2010) postulated a westward-dipping ramp detachment structure from the upper South American crust to the flat slab at 60 km which Marot et al. (2014) associate with fluids migrating from the plate interface to the continental crust resulting in locally higher Vp/Vs ratios in the forearc crust. Marot et al. (2014) also suggest that detachment faults like this may be occurring throughout the continental mantle. Ammirati et al. (2016) infer a westward dipping thrust fault between the Chilenia and Cuyania terranes down to 40 km depth that accommodates crustal deformation which may be linked to an east dipping shear zone that extends down to the Moho. Linkimer et al. (2020) connect this shear zone to an eastward-dipping paleosuture of a Gondwana subduction zone, which may also allow for hydration of the upper mantle. The presence and reactivation of such paleosutures and faults in the region (e.g., Ramos et al., 2002; Alvarado et al., 2005) can act as zones of weakness and potential conduits of relatively high permeability. Finally, bathymetric highs can also play a role in creating and reactivating faults and fracture networks as a they move through the subduction channel (Dominguez et al., 1998;2000; Wang & Bilek, 2011; Rosenbaum & Mo, 2011; Marcaillou et al., 2016, Ruh et al., 2016).

8 Conclusions

Application of an automated catalogue generation algorithm (REST) to seismic data from the SIEMBRA and ESP networks resulted in 35,924 well recorded hypocenters and 12,172 focal mechanisms for events in the region of the Pampean flat slab. A comparison of the automated catalogue with a carefully curated manually generated one shows that, in addition to producing many more observations, the accuracy of picks is at least as good as, if not better than, manual picks. Many of the events in the selective catalogue were associated with the subducted Juan Fernandez Ridge, which is often presumed to play a major role in maintaining the shallow dip of the Nazca plate here. These events also define a series of lineaments that splay from the main trend of the JFR. Inspection of the bathymetry of the Nazca plate shows a strong correlation between these lineaments and minor ridges north of the JFR. Several of the features in the JFR concentration at depth strongly correlate with patterns of seismicity seen in the South American crust directly above, suggesting a genetic relation between the two. We propose that this correlation is caused by the migration of volatiles, either as water or carbon dioxide, from the subducted ridges to the crust, increasing pore pressure and essentially fracking the crust.

Data Availability Statement

Seismic data from the SIEMBRA, ESP, CHARGE, and CHARSME deployments are available via the IRIS Data Management Center (https://ds.iris.edu/ds/nodes/dmc/). Data used to plot bathymetry is available from the General Bathymetric Chart of the Oceans (GEBCO) website (https://www.gebco.net). The automated earthquake catalogues are openly available in Zenodo (the SIEMBRA/ESP catalogue from https://doi.org/10.5281/zenodo.7863955 and the CHARGE and CHARSME/CSN catalogues from https://doi.org/10.5281/zenodo.7864070).

Acknowledgements

This project was supported by National Science Foundation (NSF) grants EAR-2027496 and EAR-2021040. Thanks to Leopolt Linkimer for providing us the arrival time catalogue and wavespeed model that we used to test the accuracy of the REST generated catalogue and to Mauro Saez for his help in project administration. The data collected by PASSCAL deployments in Argentina were provided by the IRIS Data Management Center. Some of the figures were made with PyGMT (Uieda et al., 2021) and Plotly (https://plot.ly) in Jupyter notebook (Kluyver et al., 2021).

References

Alvarado, P., & Beck, S. (2006). Source characterization of the San Juan (Argentina) crustal earthquakes of 15 January 1944 (MW 7.0) and 11 June 1952 (MW 6.8). *Earth and Planetary Science Letters*, *243* (3-4), 615-631. https://doi.org/10.1016/j.epsl.2006.01.015

Alvarado, P., Beck, S., & Zandt, G. (2007). Crustal structure of the south-central Andes Cordillera and backarc region from regional waveform modelling. *Geophysical Journal International*, *170*(2), 858-875. https://doi.org/10.1111/j.1365-246X.2007.03452.x

Alvarado, P., Pardo, M., Gilbert, H., Miranda, S., Anderson, M., Saez, M., & Beck, S. (2009). Flat-slab subduction and crustal models for the seismically active Sierras Pampeanas region of Argentina. *Backbone of the Americas: Shallow Subduction, Plateau Uplift, and Ridge and Terrane Collision*, *204*, 261-278. https://doi.org/10.1130/2009.1204(12)

Ammirati, J. B., Alvarado, P., & Beck, S. (2015). A lithospheric velocity model for the flat slab region of Argentina from joint inversion of Rayleigh wave phase velocity dispersion and teleseismic receiver functions. *Geophysical Journal International*, *202*(1), 224-241. https://doi.org/10.1093/gji/ggv140

Ammirati, J. B., Luján, S. P., Alvarado, P., Beck, S., Rocher, S., & Zandt, G. (2016). High-resolution images above the Pampean flat slab of Argentina (31–32 S) from local receiver functions: Implications on regional tectonics. *Earth and Planetary Science Letters*, *450*, 29-39. https://doi.org/10.1016/j.epsl.2016.06.018

Anderson, M., Alvarado, P., Zandt, G., & Beck, S. (2007). Geometry and brittle deformation of the subducting Nazca Plate, Central Chile and Argentina. *Geophysical Journal International*, *171*(1), 419-434. https://doi.org/10.1111/j.1365-246X.2007.03483.x

Beck, S. L., & Zandt, G. (2002). The nature of orogenic crust in the central Andes. *Journal of Geophysical Research: Solid Earth*, *107*(B10), ESE-7. https://doi.org/10.1029/2000JB000124

Beck, S.L. & Zandt, G. (2007). *Lithospheric structure and deformation of the flat slab region of Argentina* [Data set]. International Federation of Digital Seismograph Networks. https://doi.org/10.7914/SN/ZL_2007

Beck, S. L., Zandt, G., Ward, K. M., & Scire, A. (2015). Multiple styles and scales of lithospheric foundering beneath the Puna Plateau, central Andes. In *Geodynamics of a cordilleran orogenic system: The central Andes of Argentina and northern Chile: Geological society of America memoir* (Vol. 212, pp. 43–60). Geological Society of America, Inc. https://doi.org/10.1130/2015.1212(03)

Bello-González, J. P., Contreras-Reyes, E., & Arriagada, C. (2018). Predicted path for hotspot tracks off South America since Paleocene times: Tectonic implications of ridge-trench collision along the Andean margin. *Gondwana Research*, *64*, 216-234. https://doi.org/10. 1016/j.gr.2018.07.008

Bianchi, M., Heit, B., Jakovlev, A., Yuan, X., Kay, S. M., Sandvol, E., Alonso, R.N., Coira, B., Brown, L., Kind, R., & Comte, D. (2013). Teleseismic tomography of the southern Puna plateau in Argentina and adjacent regions. *Tectonophysics*, *586*, 65-83. https://doi.org/ 10.1016/j.tecto.2012.11.016

Bonnet, G., Agard, P., Angiboust, S., Fournier, M., & Omrani, J. (2019). No large earthquakes in fully exposed subducted seamount. *Geology*, *47*(5), 407-410. https://doi.org/10.1130/ G45564.1

Booker, J. R., Favetto, A., & Pomposiello, M. C. (2004). Low electrical resistivity associated with plunging of the Nazca flat slab beneath Argentina. *Nature*, *429*(6990), 399-403. https://doi.org/10.1038/nature02565

Burd, A. I., Booker, J. R., Mackie, R., Pomposiello, C., & Favetto, A. (2013). Electrical conductivity of the Pampean shallow subduction region of Argentina near 33 S: Evidence for a slab window. *Geochemistry, Geophysics, Geosystems*, *14*(8), 3192-3209. https://doi. org/10.1002/ggge.20213

Cahill, T., & Isacks, B. L. (1992). Seismicity and shape of the subducted Nazca plate. *Journal of Geophysical Research: Solid Earth*, *97*(B12), 17503-17529. https://doi.org/10.1029/ 92JB00493

912 Capaldi, T. N., Horton, B. K., McKenzie, N. R., Mackaman-Lofland, C., Stockli, D. F., Ortiz,
913 G., & Alvarado, P. (2020). Neogene retroarc foreland basin evolution, sediment
914 provenance, and magmatism in response to flat slab subduction, western
915 Argentina. *Tectonics*, *39*(7), e2019TC005958. https://doi.org/10.1029/2019TC005958
916 Chesley, C., Naif, S., Key, K., & Bassett, D. (2021). Fluid-rich subducting topography
917 generates anomalous forearc porosity. *Nature*, *595*(7866), 255-260.
918 https://doi.org/10.1038/s41586-021-03619-8
919 Comte, D., Farías, M., Roecker, S. W., & Brandon, M. T. (2017). Dense and Dry Mantle
920 Between the Continental Crust and the Oceanic Slab: Folding, Faulting and Tearing
921 in the Slab in the Pampean Flat Slab, Southern Central Andes Evidenced by 3D
922 Body Wave Tomography Along the 2015 Illapel, Chile Earthquake Rupture Area.
923 In *AGU Fall Meeting Abstracts* (Vol. 2017, pp. T23D-0638).
924 Comte, D., Farias, M., Roecker, S., & Russo, R. (2019). The nature of the subduction wedge
925 in an erosive margin: Insights from the analysis of aftershocks of the 2015 Mw 8.3
926 Illapel earthquake beneath the Chilean Coastal Range. *Earth and Planetary Science*
927 *Letters*, *520*, 50-62. https://doi.org/10.1016/j.epsl.2019.05.033
928 Comte, D., Farías, M., Calle-Gardella, D., Navarro-Aranguiz, A., Roecker, S., & Rietbrock,
929 A. (2023). Anomalous intraslab structure revealed by the analysis of aftershocks of
930 the Mw 6.7 Coquimbo-La Serena earthquake of 20 January
931 2019. *Tectonophysics*, *846*, 229660. https://doi.org/10.1016/j.tecto.2022.229660
932 Contreras-Reyes, E., & Carrizo, D. (2011). Control of high oceanic features and subduction
933 channel on earthquake ruptures along the Chile–Peru subduction zone. *Physics of*
934 *the Earth and Planetary Interiors*, *186*(1-2), 49-58.
935 https://doi.org/10.1016/j.pepi.2011.03.002
936 Clarke, A. P., Vannucchi, P., & Morgan, J. (2018). Seamount chain–subduction zone
937 interactions: Implications for accretionary and erosive subduction zone
938 behavior. *Geology*, *46*(4), 367-370. https://doi.org/10.1130/G40063.1
939 DeCelles, P. G., Carrapa, B., Horton, B. K., McNabb, J., Gehrels, G. E., Boyd, J., Ducea,
940 M.N., & Kapp, P. A. (2015). The Miocene Arizaro Basin, central Andean hinterland:
941 Response to partial lithosphere removal. In *Geodynamics of a cordilleran orogenic*
942 *system: The central Andes of Argentina and northern Chile: Geological society of*
943 *America memoir* (Vol. 212, pp. 359-386). Geological Society of America, Inc.
944 https://doi.org/10.1130/ 2015.1212(18)
945 Devey, C. W., Hémond, C., & Stoffers, P. (2000). Metasomatic reactions between carbonated
946 plume melts and mantle harzburgite: the evidence from Friday and Domingo
947 Seamounts (Juan Fernandez chain, SE Pacific). *Contributions to Mineralogy and*
948 *Petrology*, *139*, 68-84. https://doi.org/10.1007/s004100050574
949 Devey, C. W., Greinert, J., Boetius, A., Augustin, N., & Yeo, I. (2021). How volcanically
950 active is an abyssal plain? Evidence for recent volcanism on 20 Ma Nazca Plate
951 seafloor. *Marine Geology*, *440*, 106548. https://doi.org/10.1016/j.margeo.2021.106548
952 Dominguez, S., Lallemand, S. E., Malavieille, J., & von Huene, R. (1998). Upper plate
953 deformation associated with seamount subduction. *Tectonophysics*, *293*(3-4), 207-
954 224. https://doi.org/10.1016/S0040-1951(98)00086-9
955 Dominguez, S., Malavieille, J., & Lallemand, S. E. (2000). Deformation of accretionary
956 wedges in response to seamount subduction: Insights from sandbox
957 experiments. *Tectonics*, *19*(1), 182-196. https://doi.org/10.1029/1999TC900055

Ducea, M. N., Seclaman, A. C., Murray, K. E., Jianu, D., & Schoenbohm, L. M. (2013). Mantle-drip magmatism beneath the Altiplano-Puna plateau, central Andes. *Geology*, *41*(8), 915-918. https://doi.org/10.1130/G34509.1

Ellis, S., Fagereng, Å., Barker, D., Henrys, S., Saffer, D., Wallace, L., Williams, C., & Harris, R. (2015). Fluid budgets along the northern Hikurangi subduction margin, New Zealand: The effect of a subducting seamount on fluid pressure. *Geophysical Journal International*, *202*(1), 277-297. https://doi.org/10.1093/gji/ggv127

Espurt, N., Funiciello, F., Martinod, J., Guillaume, B., Regard, V., Faccenna, C., & Brusset, S. (2008). Flat subduction dynamics and deformation of the South American plate: Insights from analog modeling. *Tectonics*, *27*(3), TC3011. https://doi.org/10.1029/2007TC002175

Famin, V., Nakashima, S., Boullier, A. M., Fujimoto, K., & Hirono, T. (2008). Earthquakes produce carbon dioxide in crustal faults. *Earth and Planetary Science Letters*, *265*(3-4), 487-497. https://doi.org/10.1016/j.epsl.2007.10.041

Farías, M., Comte, D., Charrier, R., Martinod, J., David, C., Tassara, A., Tapia, F., & Fock, A. (2010). Crustal-scale structural architecture in central Chile based on seismicity and surface geology: Implications for Andean mountain building. *Tectonics*, *29*(3), TC3006. https://doi.org/10. 1029/2009TC002480

Fromm, R., Alvarado, P., Beck, S. L., & Zandt, G. (2006). The April 9, 2001 Juan Fernández Ridge (M w 6.7) tensional outer-rise earthquake and its aftershock sequence. *Journal of Seismology*, *10*, 163-170. https://doi.org/10.1007/s10950-006-9013-3

Gans, C. R., Beck, S. L., Zandt, G., Gilbert, H., Alvarado, P., Anderson, M., & Linkimer, L. (2011). Continental and oceanic crustal structure of the Pampean flat slab region, western Argentina, using receiver function analysis: new high-resolution results. *Geophysical Journal International*, *186*(1), 45-58. https://doi.org/10.1111/j.1365-246X.2011.05023.x

Galvez, M. E., Beyssac, O., Martinez, I., Benzerara, K., Chaduteau, C., Malvoisin, B., & Malavieille, J. (2013). Graphite formation by carbonate reduction during subduction. *Nature Geoscience*, *6*(6), 473-477. https://doi.org/10.1038/ngeo1827

GEBCO Compilation Group (2022). The GEBCO_2022 Grid - a continuous terrain model of the global oceans and land [Data set]. https://doi.org/10.5285/e0f0bb80-ab44-2739-e053-6c86abc0289c

Gerya, T. V., Fossati, D., Cantieni, C., & Seward, D. (2009). Dynamic effects of aseismic ridge subduction: numerical modelling. *European Journal of Mineralogy*, *21*(3), 649-661. https://doi.org/10.1127/0935-1221/2009/0021-1931

Gilbert, H., Beck, S., & Zandt, G. (2006). Lithospheric and upper mantle structure of central Chile and Argentina. *Geophysical Journal International*, *165*(1), 383-398. https://doi.org/10. 1111/j.1365-246X.2006.02867.x

Gilbert, H. (2008). *Eastern Sierras Pampeanas, Lithospheric Structure above the variably dipping Nazca Slab* [Data set]. International Federation of Digital Seismograph Networks. https://doi.org/10.7914/SN/XH_2008

Gómez, J., Schobbenhaus, C. & Montes, N.E., compilers. (2019). *Geological map of South America 2019. Scale 1:5 000 000* [Data set]. Commission for the Geological map of the World (CGMW), Colombian Geological Survey and Geological Survey of Brazil. https://doi.org/10.32685/10.143.2019.929

González-Menéndez, L., Gallastegui, G., Cuesta, A., Heredia, N., & Rubio-Ordóñez, A. (2013). Petrogenesis of Early Paleozoic basalts and gabbros in the western Cuyania

terrane: Constraints on the tectonic setting of the southwestern Gondwana margin (Sierra del Tigre, Andean Argentine Precordillera). *Gondwana Research*, *24*(1), 359-376. https://doi.org/10. 1016/j.gr.2012.09.011

Goss, A. R., Kay, S. M., & Mpodozis, C. (2013). Andean adakite-like high-Mg andesites on the northern margin of the Chilean–Pampean flat-slab (27–28 · 5° S) associated with frontal arc migration and fore-arc subduction erosion. *Journal of Petrology*, *54*(11), 2193-2234. https://doi.org/10.1093/petrology/egt044

Graveleau, F., Malavieille, J., & Dominguez, S. (2012). Experimental modelling of orogenic wedges: A review. *Tectonophysics*, *538*, 1-66. https://doi.org/10.1016/j.tecto.2012.01.027

Gunatilake, T., & Miller, S. A. (2022). Spatio-temporal complexity of aftershocks in the Apennines controlled by permeability dynamics and decarbonization. *Journal of Geophysical Research: Solid Earth*, *127*(6), e2022JB024154. https://doi.org/10.1029/2022JB024154

Hacker, B. R., Peacock, S. M., Abers, G. A., & Holloway, S. D. (2003). Subduction factory 2. Are intermediate-depth earthquakes in subducting slabs linked to metamorphic dehydration reactions?. *Journal of Geophysical Research: Solid Earth*, *108*(B1), 2030. https://doi.org/10.1029/2001JB001129

Hampel, A., Kukowski, N., Bialas, J., Huebscher, C., & Heinbockel, R. (2004). Ridge subduction at an erosive margin: The collision zone of the Nazca Ridge in southern Peru. *Journal of Geophysical Research: Solid Earth*, *109*(B2), B02101. https://doi.org/10.1029/ 2003JB002593

Hayes, G., 2018, Slab2 - A Comprehensive Subduction Zone Geometry Model: U.S. Geological Survey data release, https://doi.org/10.5066/F7PV6JNV.

Hebbeln, D., Marchant, M., Freudenthal, T., & Wefer, G. (2000). Surface sediment distribution along the Chilean continental slope related to upwelling and productivity. *Marine Geology*, *164*(3-4), 119-137. https://doi.org/10.1016/S0025-3227(99)00129-2

Jones, A. P., Genge, M., & Carmody, L. (2013). Carbonate melts and carbonatites. *Reviews in Mineralogy and Geochemistry*, *75*(1), 289-322. https://doi.org/10.2138/rmg.2013.75.10

Kay, R. W., & Kay, S. M. (1993). Delamination and delamination magmatism. *Tectonophysics*, *219*(1-3), 177-189. https://doi.org/10.1016/0040-1951(93)90295-U

Kay, S. M., & Mpodozis, C. (2002). Magmatism as a probe to the Neogene shallowing of the Nazca plate beneath the modern Chilean flat-slab. *Journal of South American Earth Sciences*, *15*(1), 39-57. https://doi.org/10.1016/S0895-9811(02)00005-6

Kluyver, T., Ragan-Kelley, B., Pérez, F., Granger, B. E., Bussonnier, M., Frederic, J., Kelley, K., Hamrick, J.B., Grout, J., Corlay, S., Ivanov, P., Avila, D., Abdalla, S., Willing, C., & Jupyter Development Team. (2016). Jupyter Notebooks-a publishing format for reproducible computational workflows. In *Positioning and power in academic publishing: Players, agents and agendas* (pp. 87-90). IOS Press. https://doi.org/10.3233/978-1-61499-649-1-87

Kopp, H., Flueh, E. R., Papenberg, C., & Klaeschen, D. (2004). Seismic investigations of the O'Higgins Seamount Group and Juan Fernández Ridge: Aseismic ridge emplacement and lithosphere hydration. *Tectonics*, *23*(2), TC2009. https://doi.org/10.1029/2003TC001590

Kushnir, A. F., Lapshin, V. M., Pinsky, V. I., & Fyen, J. (1990). Statistically optimal event detection using small array data. *Bulletin of the Seismological Society of America*, *80*(6B), 1934-1950. https://doi.org/10.1785/BSSA08006B1934

Lanza, F., Chamberlain, C. J., Jacobs, K., Warren-Smith, E., Godfrey, H. J., Kortink, M., Thurber, C.H., Savage, M.K., Townend, J., Roecker, S., & Eberhart-Phillips, D. (2019). Crustal fault connectivity of the Mw 7.8 2016 Kaikōura earthquake constrained by aftershock relocations. *Geophysical Research Letters*, *46*(12), 6487-6496. https://doi.org/10.1029/ 2019GL082780

Lara, L. E., Reyes, J., Jicha, B. R., & Díaz-Naveas, J. (2018). 40Ar/39Ar geochronological constraints on the age progression along the Juan Fernández Ridge, SE Pacific. *Frontiers in Earth Science*, *6*, 194. https://doi.org/10.3389/feart.2018.00194

Levina, M., Horton, B. K., Fuentes, F., & Stockli, D. F. (2014). Cenozoic sedimentation and exhumation of the foreland basin system preserved in the Precordillera thrust belt (31–32 S), southern central Andes, Argentina. *Tectonics*, *33*(9), 1659-1680. https://doi.org/10 .1002/2013TC003424

Linkimer, L., Beck, S., Zandt, G., Alvarado, P., Anderson, M., Gilbert, H., & Zhang, H. (2020). Lithospheric structure of the Pampean flat slab region from double-difference tomography. *Journal of South American Earth Sciences*, *97*, 102417. https://doi.org/10.1016/j.jsames.2019.102417

Li, Z., Roecker, S., Wei, B., Wang, H., Schelochkov, G. & Bragin, V. (2009). Tomographic image of the crust and upper mantle beneath the western Tien Shan from the MANAS broadband deployment: possible evidence for lithospheric delamination, Tectonophysics, 477(1–2), 49–57. https://doi.org/10.1016/j.tecto.2009.05.007

Littel, G. F., Bostock, M. G., Schaeffer, A., & Roecker, S. (2023). Microplate evolution in the Queen Charlotte triple junction & Explorer region: New insights from microseismicity. Tectonics, in press.

Manea, V. C., Manea, M., Ferrari, L., Orozco-Esquivel, T., Valenzuela, R. W., Husker, A., & Kostoglodov, V. (2017). A review of the geodynamic evolution of flat slab subduction in Mexico, Peru, and Chile. *Tectonophysics*, *695*, 27-52. https://doi.org/10.1016/j.tecto.2016. 11.037

Marcaillou, B., Collot, J. Y., Ribodetti, A., d'Acremont, E., Mahamat, A. A., & Alvarado, A. (2016). Seamount subduction at the North-Ecuadorian convergent margin: Effects on structures, inter-seismic coupling and seismogenesis. *Earth and Planetary Science Letters*, *433*, 146-158. https://doi.org/10.1016/j.epsl.2015.10.043

Marot, M., Monfret, T., Pardo, M., Ranalli, G., & Nolet, G. (2013). A double seismic zone in the subducting Juan Fernandez Ridge of the Nazca Plate (32 S), central Chile. *Journal of Geophysical Research: Solid Earth*, *118*(7), 3462-3475. https://doi.org/10.1002/jgrb. 50240

Marot, M., Monfret, T., Gerbault, M., Nolet, G., Ranalli, G., & Pardo, M. (2014). Flat versus normal subduction zones: a comparison based on 3-D regional traveltime tomography and petrological modelling of central Chile and western Argentina (29–35 S). *Geophysical Journal International*, *199*(3), 1633-1654. https://doi.org/10.1093/gji/ggu355

Martínez, F., Arriagada, C., Valdivia, R., Deckart, K., & Peña, M. (2015). Geometry and kinematics of the Andean thick-skinned thrust systems: insights from the Chilean Frontal Cordillera (28–28.5 S), Central Andes. *Journal of South American Earth Sciences*, *64*, 307-324. https://doi.org/10.1016/j.jsames.2015.05.001

Martinod, J., Funiciello, F., Faccenna, C., Labanieh, S., & Regard, V. (2005). Dynamical effects of subducting ridges: insights from 3-D laboratory models. *Geophysical Journal International*, *163*(3), 1137-1150. https://doi.org/10.1111/j.1365-246X.2005.02797.x

Meade, C., & Jeanloz, R. (1991). Deep-focus earthquakes and recycling of water into the Earth's mantle. Science, 252(5002), 68-72. https://doi.org/10.1126/science.252.5002.68

Merrill, R. J., Bostock, M. G., Peacock, S. M., Schaeffer, A. J., & Roecker, S. W. (2022). Complex structure in the Nootka Fault zone revealed by double-difference tomography and a new earthquake catalog. *Geochemistry, Geophysics, Geosystems*, *23*(2), e2021GC010205. https:// doi.org/10.1029/2021GC010205

Miller, S. A., Collettini, C., Chiaraluce, L., Cocco, M., Barchi, M., & Kaus, B. J. (2004). Aftershocks driven by a high-pressure CO2 source at depth. *Nature*, *427*(6976), 724-727. https://doi.org/10.1038/nature02251

Mochizuki, K., Yamada, T., Shinohara, M., Yamanaka, Y., & Kanazawa, T. (2008). Weak interplate coupling by seamounts and repeating M~ 7 earthquakes. *Science*, *321*(5893), 1194-1197. https://doi.org/10.1126/science.1160250

Murray, K. E., Ducea, M. N., Schoenbohm, L., DeCelles, P. G., Carrapa, B., & Kapp, P. A. (2015). Foundering-driven lithospheric melting: The source of central Andean mafic lavas on the Puna Plateau (22 S–27 S). In *Geodynamics of a cordilleran orogenic system: The central Andes of Argentina and northern Chile: Geological society of America memoir*. (Vol. 212, pp. 139-166). Geological Society of America. https://doi.org/10.1130/2015.1212(08)

Navarro-Aránguiz, A., Comte, D., Farías, M., Roecker, S., Calle-Gardella, D., Zhang, H., Gao, L., & Rietbrock, A. (2022). Subduction erosion and basal accretion in the Central Chile subduction wedge inferred from local earthquake tomography. *Journal of South American Earth Sciences*, *115*, 103765. https://doi.org/10.1016/j.jsames.2022.103765

Nikulin, A., Bourke, J. R., Domino, J. R., & Park, J. (2019). Tracing geophysical indicators of fluid-induced serpentinization in the Pampean flat slab of Central Chile. *Geochemistry, Geophysics, Geosystems*, *20*(9), 4408-4425. https://doi.org/10.1029/2019GC008491

Pardo, M., Monfret, T., Vera, E., Yanez, G., Bonvalot, S., Gabalda, G., Eisenberg, A., Triep, E., Hustedt, B, & Bethoux, N. (2003). The 2002-2003 CHARSME Experiment: Preliminary Results. In *AGU Fall Meeting Abstracts* (Vol. 2003, pp. S41D-0126).

Paul, S. A., Haeckel, M., Bau, M., Bajracharya, R., & Koschinsky, A. (2019). Small-scale heterogeneity of trace metals including REY in deep-sea sediments and pore waters of the Peru Basin, southeastern equatorial Pacific. *Biogeosciences (BG)*, *16*(24), 4829-4849. https://doi.org/10.5194/bg-2019-274

Perkins, G. B., Sharp, Z. D., & Selverstone, J. (2006). Oxygen isotope evidence for subduction and rift-related mantle metasomatism beneath the Colorado Plateau–Rio Grande rift transition. *Contributions to Mineralogy and Petrology*, *151*, 633-650. https://doi.org/10. 1007/s00410-006-0075-6

Pfiffner, O. A. (2017). Thick-skinned and thin-skinned tectonics: A global perspective. *Geosciences*, *7*(3), 71. https://doi.org/10.3390/geosciences7030071

Pisarenko, V. F., Kushnir, A. F., & Savin, I. V. (1987). Statistical adaptive algorithms for estimation of onset moments of seismic phases. *Physics of the Earth and Planetary Interiors*, *47*, 4-10. https://doi.org/10.1016/0031-9201(87)90062-8

1148 Pommier, A., & Evans, R. L. (2017). Constraints on fluids in subduction zones from
1149 electromagnetic data. *Geosphere*, *13*(4), 1026-1041.
1150 https://doi.org/10.1130/GES01473.1
1151 Porter, R., Gilbert, H., Zandt, G., Beck, S., Warren, L., Calkins, J., Alvarado, P., &
1152 Anderson, M. (2012). Shear wave velocities in the Pampean flat-slab region from
1153 Rayleigh wave tomography: Implications for slab and upper mantle
1154 hydration. *Journal of Geophysical Research: Solid Earth*, *117*(B11),
1155 B11301. https://doi.org/10.1029/2012JB009350
1156 Ramos, V. A., Cegarra, M., & Cristallini, E. (1996). Cenozoic tectonics of the High Andes of
1157 west-central Argentina (30–36 S latitude). *Tectonophysics*, *259*(1-3), 185-200.
1158 https://doi.org/ 10.1016/0040-1951(95)00064-X
1159 Ramos, V. A., Cristallini, E. O., & Pérez, D. J. (2002). The Pampean flat-slab of the Central
1160 Andes. *Journal of South American Earth Sciences*, *15*(1), 59-78.
1161 https://doi.org/10.1016/ S0895-9811(02)00006-8
1162 Ranero, C. R., Villaseñor, A., Phipps Morgan, J., & Weinrebe, W. (2005). Relationship
1163 between bend-faulting at trenches and intermediate-depth seismicity. *Geochemistry,*
1164 *Geophysics, Geosystems*, *6*(12), Q12002. https://doi.org/10.1029/2005GC000997
1165 Rawles, C., & Thurber, C. (2015). A non-parametric method for automatic determination of
1166 P-wave and S-wave arrival times: application to local micro
1167 earthquakes. *Geophysical Journal International*, *202*(2), 1164-1179.
1168 https://doi.org/10.1093/gji/ggv218
1169 Richardson, T., Gilbert, H., Anderson, M., & Ridgway, K. D. (2012). Seismicity within the
1170 actively deforming eastern Sierras Pampeanas, Argentina. *Geophysical Journal*
1171 *International*, *188*(2), 408-420. https://doi.org/10.1111/j.1365-246X.2011.05283.x
1172 Rodrigo, C., & Lara, L. E. (2014). Plate tectonics and the origin of the Juan Fernández
1173 Ridge: analysis of bathymetry and magnetic patterns. *Latin American Journal of*
1174 *Aquatic Research*, *42*(4), 907-917. http://dx.doi.org/10.3856/vol42-issue4-fulltext-15
1175 Roecker, S., Maharaj, A., Comte, D., Navarro-Aranguiz, A., & Alvarado, P. (2021,
1176 December). Imaging a Potential Lithospheric Root Trapped Above the Pampean Flat
1177 Slab. In *AGU Fall Meeting Abstracts* (Vol. 2021, pp. DI45D-0041).
1178 Roecker, S., Maharaj, A., Meyers, S., & Comte, D. (2021). Double differencing by
1179 demeaning: applications to hypocenter location and wavespeed tomography. *Bulletin*
1180 *of the Seismological Society of America*, *111*(3), 1234-1247.
1181 https://doi.org/10.1785/0120210007
1182 Rosenbaum, G., & Mo, W. (2011). Tectonic and magmatic responses to the subduction of
1183 high bathymetric relief. *Gondwana Research*, *19*(3), 571-582.
1184 https://doi.org/10.1016/j.gr.2010.10.007
1185 Ruh, J. B., Sallarès, V., Ranero, C. R., & Gerya, T. (2016). Crustal deformation dynamics
1186 and stress evolution during seamount subduction: High-resolution 3-D numerical
1187 modeling. *Journal of Geophysical Research: Solid Earth*, *121*(9), 6880-6902.
1188 https://doi.org/10.1002/2016JB013250
1189 Schoenbohm, L. M., Carrapa, B., DeCelles, P. G., Ducea, M. N., & Kapp, P. A. (2015).
1190 Miocene–Pliocene shortening, extension, and mafic magmatism support small-scale
1191 lithospheric foundering in the central Andes, NW Argentina. In *Geodynamics of a*
1192 *cordilleran orogenic system: The central Andes of Argentina and northern Chile:*
1193 *Geological society of America memoir* (Vol. 212, pp. 167-180). Geological Society of
1194 America, Inc. https://doi.org/10.1130/2015.1212(09)

Scholz, C. H., & Small, C. (1997). The effect of seamount subduction on seismic coupling. *Geology*, *25*(6), 487-490. https://doi.org/10.1130/00917613(1997)025<0487:TEOSSO>2.3.CO;2

Selway, K. (2014). On the causes of electrical conductivity anomalies in tectonically stable lithosphere. *Surveys in Geophysics*, *35*, 219-257. https://doi.org/10.1007/s10712-013-9235-1

Skinner, S. M., & Clayton, R. W. (2013). The lack of correlation between flat slabs and bathymetric impactors in South America. *Earth and Planetary Science Letters*, *371*, 1-5. https://doi.org/10.1016/j.epsl.2013.04.013

Smalley Jr, R. F., & Isacks, B. L. (1987). A high-resolution local network study of the Nazca Plate Wadati-Benioff Zone under western Argentina. *Journal of Geophysical Research: Solid Earth*, *92*(B13), 13903-13912. https://doi.org/10.1029/JB092iB13p13903

Snoke, J. A (2003). FOCMEC: Focal mechanism determinations. In *International handbook of earthquake and engineering seismology* (Vol. 81, pp. 1629-1630). Academic Press. https://doi.org/10.1016/S0074-6142(03)80291-7

Staudigel, H., Koppers, A. A., Plank, T. A., & Hanan, B. B. (2010). Seamounts in the subduction factory. *Oceanography*, *23*(1), 176-181. http://www.jstor.org/stable/24861082

Stern, C. R. (2020). The role of subduction erosion in the generation of Andean and other convergent plate boundary arc magmas, the continental crust and mantle. *Gondwana Research*, *88*, 220-249. https://doi.org/10.1016/j.gr.2020.08.006

Tarantola, A., & Valette, B. (1982). Inverse problems = quest for information. *Journal of Geophysics*, *50*(1), 159-170.

Tilmann, F., Zhang, Y., Moreno, M., Saul, J., Eckelmann, F., Palo, M., Deng, Z., Babeyko, A., Chen, K., Báez, J.C. and Schurr, B., Wang, R., & Dahm, T. (2016). The 2015 Illapel earthquake, central Chile: A type case for a characteristic earthquake?. *Geophysical Research Letters*, *43*(2), 574-583. https://doi.org/10.1002/2015GL066963

Uieda, L., Tian, D., Leong, W. J., Toney, L., Schlitzer, W., Grund, M., Newton, D., Ziebarth, M., Jones, M., & Wessel, P. (2021). *PyGMT: A Python interface for the generic mapping tools* [Computer software]. Zenodo. https://doi.org/10.5281/zenodo.4522136

van Hunen, J., van den BERG, A. P., & Vlaar, N. J. (2002). On the role of subducting oceanic plateaus in the development of shallow flat subduction. *Tectonophysics*, *352*(3-4), 317-333. https://doi.org/10.1016/S0040-1951(02)00263-9

van Hunen, J., van den Berg, A. P., & Vlaar, N. J. (2004). Various mechanisms to induce present-day shallow flat subduction and implications for the younger Earth: a numerical parameter study. *Physics of the Earth and* Villagomez, D. R., Toomey, D. R., Geist, D. J., Hooft, E. E., & Solomon, S. C. (2014). Mantle flow and multistage melting beneath the Gal.pagos hotspot revealed by seismic imaging. Nature Geoscience, 7(2), 151-156. https://doi.org/10.1038/ngeo2062

Venerdini, A., Alvarado, P., Ammirati, J. B., Podesta, M., López, L., Fuentes, F., Linkimer, L., & Beck, S. (2020). Crustal seismicity in the Andean Precordillera of Argentina using seismic broadband data. *Tectonophysics*, *786*, 228450. https://doi.org/10.1016/j.tecto.2020.228450

von Huene, R., Corvalán, J., Flueh, E. R., Hinz, K., Korstgard, J., Ranero, C. R., & Weinrebe, W. (1997). Tectonic control of the subducting Juan Fernández Ridge on

1243 the Andean margin near Valparaiso, Chile. *Tectonics*, *16*(3), 474-
1244 488. https://doi.org/10.1029/96TC03703
1245 Vujovich, G. I., van Staal, C. R., & Davis, W. (2004). Age constraints on the tectonic
1246 evolution and provenance of the Pie de Palo Complex, Cuyania composite terrane,
1247 and the Famatinian Orogeny in the Sierra de Pie de Palo, San Juan,
1248 Argentina. *Gondwana Research*, *7*(4), 1041-1056. https://doi.org/10.1016/S1342-
1249 937X(05)71083-2
1250 Wagner, L. S., Beck, S., & Zandt, G. (2005). Upper mantle structure in the south central
1251 Chilean subduction zone (30 to 36 S). *Journal of Geophysical Research: Solid*
1252 *Earth*, *110*(B1), B01308. https://doi.org/10.1029/2004JB003238
1253 Wagner, L. S., Beck, S., Zandt, G., & Ducea, M. N. (2006). Depleted lithosphere, cold,
1254 trapped asthenosphere, and frozen melt puddles above the flat slab in central Chile
1255 and Argentina. *Earth and Planetary Science Letters*, *245*(1-2), 289-301.
1256 https://doi.org/10. 1016/j.epsl.2006.02.014
1257 Wagner, L. S., Anderson, M. L., Jackson, J. M., Beck, S. L., & Zandt, G. (2008). Seismic
1258 evidence for orthopyroxene enrichment in the continental
1259 lithosphere. *Geology*, *36*(12), 935-938. https://doi.org/10.1130/G25108A.1
1260 Waldhauser, F., & Ellsworth, W. L. (2000). A double-difference earthquake location
1261 algorithm: Method and application to the northern Hayward fault,
1262 California. *Bulletin of the seismological society of America*, *90*(6), 1353-1368.
1263 https://doi.org/10.1785/0120000006
1264 Wang, K., & Bilek, S. L. (2011). Do subducting seamounts generate or stop large
1265 earthquakes?. *Geology*, *39*(9), 819-822. https://doi.org/10.1130/G31856.1
1266 Wang, H., Currie, C. A., & DeCelles, P. G. (2015). Hinterland basin formation and
1267 gravitational instabilities in the central Andes: Constraints from gravity data and
1268 geodynamic models. *In Geodynamics of a cordilleran orogenic system: The central*
1269 *Andes of Argentina and northern Chile: Geological society of America memoir* (Vol.
1270 212, pp. 387-406). Geological Society of America, Inc.
1271 https://doi.org/10.1130/2015.1212(19)
1272 Wang, Z., & Lin, J. (2022). Role of fluids and seamount subduction in interplate coupling
1273 and the mechanism of the 2021 Mw 7.1 Fukushima-Oki earthquake, Japan. *Earth*
1274 *and Planetary Science Letters*, *584*, 117439.
1275 https://doi.org/10.1016/j.epsl.2022.117439
1276 Watts, A. B., Koppers, A. A., & Robinson, D. P. (2010). Seamount subduction and
1277 earthquakes. *Oceanography*, *23*(1), 166-173. http://www.jstor.org/stable/24861080
1278 Yáñez, G. A., Ranero, C. R., von Huene, R., & Díaz, J. (2001). Magnetic anomaly
1279 interpretation across the southern central Andes (32–34 S): The role of the Juan
1280 Fernández Ridge in the late Tertiary evolution of the margin. *Journal of Geophysical*
1281 *Research: Solid Earth*, *106*(B4), 6325-6345. https://doi.org/10.1029/2000JB900337
1282 Yáñez, G., Cembrano, J., Pardo, M., Ranero, C., & Selles, D. (2002). The Challenger–Juan
1283 Fernández–Maipo major tectonic transition of the Nazca–Andean subduction system
1284 at 33–34 S: geodynamic evidence and implications. *Journal of South American Earth*
1285 *Sciences*, *15*(1), 23-38. https://doi.org/10.1016/S0895-9811(02)00004-4
1286 Yang, G., Li, Y., Zhu, Z., Li, H., Tong, L., & Zeng, R. (2022). Seamount subduction and
1287 accretion in West Junggar, NW China: A review. *Geosystems and Geoenvironment*,
1288 in press https://doi.org/10.1016/j.geogeo.2022.100074
1289 Yarce, J., Sheehan, A. & Roecker, S. (2023). Temporal relationship of slow slip events and
1290 microearthquake seismicity: Insights from earthquake automatic detections in the

northern Hikurangi margin, Aotearoa New Zealand, *Geochemistry, Geophysics, and Geosystems*, in press

Zhang, H., Roecker, S., Thurber, C. H., Wang, W., & Dar, I. A. (2012). Seismic imaging of microblocks and weak zones in the crust beneath the southeastern margin of the Tibetan Plateau. In *Earth sciences* (pp. 159-202). InTech. https://doi.org/10.5772/27876

Zheng, Y., Chen, R., Xu, Z., & Zhang, S. (2016). The transport of water in subduction zones. *Science China Earth Sciences*, *59*, 651-682. https://doi.org/10.1007/s11430-015-5258-4